Tumor Suppressor p53 Restrains Cancer Cell Dissemination by Modulating Mitochondrial Dynamics

Thi Tuyet Trinh Phan[1,], Yu-Chun Lin[2], Yu-Ting Chou[3], Chien-Wei Wu[1], and Lih-Yuan Lin[1,*]**

[1] Institute of Molecular and Cellular Biology, College of Life Science, National Tsing Hua University, Hsinchu 300044, Taiwan R.O.C

[2] Institute of Molecular Medicine, College of Life Science, National Tsing Hua University, Hsinchu 300044, Taiwan R.O.C

[3] Institute of Biotechnology, College of Life Science, National Tsing Hua University, Hsinchu 300044, Taiwan R.O.C

*Corresponding author (lead contact). Tel: +886 3 574 2693 ; Email: lylin@life.nthu.edu.tw

**Corresponding author. Tel: +886 3 571 5131 #34375; Email: s107080893@m107.nthu.edu.tw

Abstract

Tumor suppressor p53 plays a central role in preventing tumorigenesis. Here, we unravel how p53 modulates mitochondrial dynamics to restrain the metastatic properties of cancer cells. p53 inhibits the mammalian target of rapamycin complex 1 (mTORC1) signaling to attenuate the protein level of mitochondrial fission process 1 (MTFP1), which fosters the pro-fission dynamin-related protein 1 (Drp1) phosphorylation. This regulatory mechanism allows p53 to restrict cell migration and invasion governed by Drp1-mediated mitochondrial fission. Downregulating p53 or elevating the molecular signature of mitochondrial fission correlates with aggressive tumor phenotypes and poor prognosis in cancer patients. Upon p53 loss, exaggerated mitochondrial fragmentation stimulates the activation of the extracellular signal-regulated kinase 1/2 (ERK1/2) signaling resulting in epithelial-to-mesenchymal transition (EMT)-like changes in cell morphology, accompanied by accelerated matrix metalloproteinase-9 (MMP9) expression and invasive cell migration. Notably, blocking the p53 deficiency-induced activation of mTORC1/MTFP1/Drp1/ERK axis completely abolishes the morphological switch, MMP9 expression, and cancer cell dissemination. Our findings unveil a hitherto unrecognized molecular mechanism underlying the metastatic phenotypes of p53-compromised cancers.

Keywords

cell dissemination; mitochondrial dynamics; MMP9; mTORC1; p53

Introduction

Metastasis is the dissemination of cancer cells from an original primary site to distant organs or tissues resulting in the formation of new tumors within the body (Fares *et al*, 2020). The metastatic cascade of solid tumors can be dissected into five sequential steps: the process initiates with local invasion across basement membrane, follows by intravasation into the blood and lymphatic vessels, continues with survival in the circulatory system, advances with extravasation from the bloodstream to distant sites, and finalizes with colonization at secondary metastatic sites (Hapach *et al*, 2019). Cell migration and invasion, which are governed by cell motility, are recognized as key parameters crucial for the initiation and progression of the metastatic cascade (Yilmaz & Christofori, 2010). Despite its importance in determining the clinical prognosis of cancer patients, little is known about the rate-limiting steps governing and/or promoting tumor cell motility and invasiveness.

Mitochondria are double membraned subcellular organelles that perform diverse functions in eukaryotic cells. Besides generating metabolic energy to power cellular functions, mitochondria participate in a multitude of vital processes regulating cellular redox, calcium homeostasis, aging, and cell death (Giorgi *et al*, 2018; Nunnari & Suomalainen, 2012). Recently, mitochondrial dynamics has been implicated in controlling the metastatic dissemination of cancer cells (Huang *et al*, 2018; Liang *et al*, 2020; Sun *et al*, 2018; Yin *et al*, 2016; Zhang *et al*, 2020; Zhao *et al*, 2013). Enforcing mitochondrial fission or inhibiting mitochondrial fusion supports cell migration, invasion, and metastasis in hepatocellular carcinoma, glioma, pancreatic, breast, and bladder cancers. Paradoxically, increased mitochondrial fission attenuates metastasis in triple-negative breast cancer (Humphries *et al*, 2020). Thus, whether mitochondrial fission or fusion advances the metastatic potential of cancer cells may be context-dependent and requires further investigation.

Mitochondrial fission and fusion processes are controlled by a conserved superfamily of dynamin-like guanosine triphosphatases (GTPases) (Westermann, 2010). Mitochondrial fusion is mediated by Mitofusin 1 (Mfn1), Mitofusin 2 (Mfn2), and Optic Atrophy 1 (Opa1). Mitochondria fission is controlled by dynamin-related protein 1 (Drp1) and its accessory receptors mitochondrial fission 1 (Fis1), mitochondrial fission factor (Mff), and mitochondrial dynamics proteins of 49 and 51 kDa (MiD49/MIEF2 and MiD51/MIEF1) (Pernas & Scorrano, 2016). Phosphorylation of Drp1 at serine 616 (S616) and serine 637 (S637) is best known for regulating Drp1 activity and mitochondrial fission. Phosphorylation of S637 on Drp1 inhibits its GTPase activity, promoting the elongation of the mitochondrial network, whereas phosphorylation of S616 on Drp1 facilitates the translocation of cytosolic Drp1 to the outer mitochondrial membrane and induces mitochondrial fragmentation (Kraus & Ryan, 2017). Because mitochondrial dynamics is tightly associated with the metastatic abilities of cancer cells, identification of additional regulators modulating mitochondrial dynamics could benefit the discovery of novel therapeutic approaches to target malignant tumors.

Mammalian target of rapamycin (mTOR) is a serine/threonine-protein kinase that functions as the catalytic subunit of two distinct multiprotein complexes, named mTOR complex 1 (mTORC1) and mTOR complex 2 (mTORC2) (Guertin & Sabatini, 2007). It has been established that mTORC1 is an important regulator of mitochondrial dynamics. mTORC1 phosphorylates 4EBPs (the translation initiation factor 4E (eIF4E)-binding proteins) and prevents it from binding eIF4E. The eIF4E can then initiate the translation of the mitochondrial fission process 1 (MTFP1). MTFP1 is a transmembrane protein locates in the mitochondrial inner membrane and facilitates Drp1-driven mitochondrial fission (Morita *et al*, 2017; Tondera *et al*, 2005). Studies have suggested mTOR activation contributes to elevated cancer migration, invasion, and metastasis (Harvey *et al*, 2019; Liu *et al*, 2006), while mTOR inhibition results in mitochondrial elongation and branching (Morita *et al*, 2013; Morita *et al.*, 2017) and the morphology can be completely

reversed by overexpressing MTFP1 (Morita *et al.*, 2017). However, the links among mTOR, metastasis, and mitochondrial dynamics have not been examined.

The tumor suppressor p53, encoded by the tumor protein p53 (*TP53*) gene, is a master regulator of multiple cell fate-determining genes and prevents the oncogenic activation of the mTOR signaling pathway (Budanov & Karin, 2008; Feng *et al*, 2007; Stambolic *et al*, 2001; Vousden & Ryan, 2009). Loss of p53 activity is a hallmark of most human tumors, affecting more than one-half of cancer cases (Joerger & Fersht, 2007). Accumulating data suggests an unconventional role of p53 in controlling cancer cell invasiveness (Powell *et al*, 2014). p53 also impacts mitochondrial integrity in response to various stresses by either regulating proteins involved in mitochondrial quality control and metabolism or maintaining the mitochondrial genomic integrity (Achanta *et al*, 2005; Nakamura & Arakawa, 2017; Park *et al*, 2016; Zhou *et al*, 2003). Nonetheless, how p53 modulates the morphological dynamics of mitochondria remains poorly understood. Moreover, whether mitochondrial dynamics is involved in p53-dependent regulation of cell motility and invasion has not been addressed.

In this study, we delineate a p53-regulated circuitry that restrains the metastatic dissemination of cancer cells and contributes to cancer phenotypes and patient prognosis. We show that p53 alleviates Drp1-driven mitochondrial fission by inhibiting the mTORC1-mediated MTFP1 protein expression. p53 deficiency-exaggerated mitochondrial fragmentation activates ERK1/2 signaling leading to remarkable changes in cell morphology and robust increases in the matrix metalloproteinase-9 (MMP9) expression and invasive cell migration. Hence, mitochondrial fission represents a driving force for signal transduction that directs cancer cell dissemination when wild-type (WT) p53 functions are impaired.

Results

Downregulation of WT p53 expression is associated with aggressive tumor phenotypes and poor prognosis

Given that *TP53* is among the most frequently altered genes in metastatic cancers (Robinson *et al*, 2017), we investigated the associations between the presence of *TP53* mutations and cancer metastases using The Cancer Genome Atlas (TCGA) Pan-Cancer (Fig 1A) and the Memorial Sloan-Kettering Integrated Mutation Profiling of Actionable Cancer Targets (MSK-IMPACT) (Fig 1B) cohorts. Results revealed that cancer patients harboring mutant (MUT) *TP53* had a higher risk of developing metastases to lymph nodes (Fig 1A, lymph node-negative (N0) vs lymph node-positive (N1+)) and distant organs (Fig 1B) as compared to those having WT *TP53*. In addition, overall survival was significantly longer in patients with WT *TP53* than in those with MUT *TP53* (Fig 1C). As emerging evidence demonstrates the important role of WT p53 in suppressing cancer metastasis (Powell *et al.*, 2014), we reasoned that the expression level of WT p53 might also be a contributing factor in determining disease aggressiveness and patient outcomes. To this end, we analyzed the levels of p53 protein expression in primary tumors from N0 and N1+ cancer patients harboring WT *TP53* using the reverse-phase protein array (RPPA) data derived from the TCGA Pan-Cancer dataset (Fig 1D). Results indicated that N1+ tumors had decreased protein levels of WT p53 as compared to those in N0 tumors. Of tumors with WT *TP53*, levels of p53 protein expression were also reduced in advanced-stage (III and IV) tumors when compared to those in the earlier-stage (I and II) tumors (Fig 1E). In line with these observations, p53 mRNA levels were significantly decreased in distant metastatic compared to those in primary melanoma (Fig EV1A). The p53 protein levels of tumors having WT *TP53* were inversely correlated with the mRNA levels of epithelial-to-mesenchymal transition (EMT)-promoting transcription factors Twist1 (Fig EV1B), Slug (Fig EV1C), and Snail (Fig EV1D), suggesting a negative impact of WT p53 on EMT, a key event that drives cancer metastasis.

Consistently, *TP53* WT tumors had lower mRNA levels of Twist1, Snail, and Slug than those in *TP53* MUT tumors (Fig EV1E). Reduced p53 protein levels were strongly correlated with impaired overall survival in cancer patients harboring WT *TP53* (Fig 1F). These data suggest that impaired expression of WT p53 is implicated in exaggerated malignant phenotypes and poor prognosis of cancer patients.

p53 silencing accelerates cancer cell migration and invasion

To validate the contribution of WT p53 in suppressing cancer dissemination, we silenced p53 in human non‑small cell lung cancer (NSCLC) A549 and human breast cancer MCF-7 cells with small interference (si)-RNAs. Both cell types express WT p53. Phase-contrast imaging indicated that p53 depletion induced significant morphological changes in both A549 and MCF-7 cells. p53-depleted cells exhibited a decrease in cell-cell adhesions, an elongated cell body, and a spindle-shaped morphology, which were much different from the high cell-cell adhesion and epithelial-like morphology in p53 WT controls (Fig 1G). Because the phenotypic switch from epithelial- to spindle-like morphology is one of the hallmarks of EMT, allowing cells to become motile and invasive, we investigated the role of p53 in regulating cell migration and invasion. As expected, single-cell tracking and wound-healing assays showed that p53 silencing stimulated A549 cell motility (Figs 1H, 1I, and EV1F). Moreover, transwell assays further confirmed that p53-silenced cells were more migratory and invasive than p53 WT controls (Fig 1K). Taken together, these results indicate that loss of WT p53 induced a more aggressive cancer cell phenotype and heightened cell motility and invasion.

p53 silencing amplifies mitochondrial fission has diagnostic and clinical implications

Our results highlight an important role of WT p53 in restraining the metastatic dissemination of cancer cells. Building on previous findings that metastasizing cancer cells need to alter their mitochondrial morphology to facilitate their motility and invasiveness (Caino *et al*, 2016; Sun *et*

al., 2018; Zhao *et al.*, 2013), we assessed the morphological dynamics of mitochondria upon WT p53 loss. Using live-cell fluorescence imaging, we observed cells harboring WT p53 have predominantly intermediate mitochondria (>78%). Upon p53 silencing, cells with fragmented mitochondria were dramatically enhanced while cells with elongated and intermediate mitochondria were drastically reduced. Mitochondria were fragmented in more than 80% of p53-depleted cells (less than 2% in p53 WT controls) (Figs 2A and 2B). These results provide strong evidence that mitochondrial dynamics is modulated by p53.

As p53 silencing amplified mitochondrial fission, we investigated the clinical significance of Drp1, a major pro-fission protein. The mRNA expression levels of Drp1 were elevated in N1+ tumors compared to those in N0 tumors (Fig 2C). Consistent with this finding, we also observed an increase in mRNA levels of Drp1 in advanced-stage (II and IV) tumors when compared to those in the earlier-stage (I and II) tumors (Fig 2D). Especially, Drp1 mRNA levels were higher in distant metastatic than in primary melanoma (Fig EV2A). Direct correlations were also found between mRNA levels of Drp1 and EMT drivers such as Twist1 (Fig EV2B) and Slug (Fig EV2C), confirming the pro-metastatic implications of Drp1 in cancers. Furthermore, high Drp1 levels significantly reduced overall survival in cancer patients (Fig 2E). These data corroborate a strong association of mitochondrial morphology with the degree of tumor malignancy and clinical outcomes in cancers.

p53 elevation promotes mitochondrial elongation accompanied by attenuated invasive cell migration

Sodium arsenite (SA) is a genotoxic agent that induces DNA damages in human cell lines (Guillamet *et al*, 2004; Schwerdtle *et al*, 2003) and elevates endogenous p53 expression (Fig EV3A). We examined the effects of SA-induced endogenous p53 upregulation on mitochondrial dynamics and the metastatic abilities of cancer cells. Although 10 μM SA was sufficient to

induce p53 expression in A549 cells (Fig EV3A), treating cells with 10, 20, or 40 μM SA did not affect cell viability and proliferation (Figs EV3B and EV3C). Furthermore, A549 cells treated with increased concentration (20 or 40 μM) of SA had higher accumulations of p53 protein. Thus, a 24-h treatment with a non-cytotoxic concentration of 20 μM SA was chosen to amplify the endogenous p53 expression in A549 cells. The expression of the endogenous p53 with and without SA induction can be effectively silenced with siRNA (Fig 3A). Critically, these treatments did not change the survival of p53-depleted cells (Fig EV3D).

We have shown that cells with p53 knockdown have decreased mitochondrial elongation and enhanced mitochondrial fragmentation (Figs 2A and 2B). In contrast, SA-elevated endogenous p53 expression promoted a robust increase in mitochondrial branching and elongation (Figs 3B and 3C). In SA-treated A549 cells, almost 80% of cells showed elongated mitochondria as compared to 20% in control cells. p53 depletion completely reversed the effects of SA on mitochondrial elongation, accompanied by enhanced mitochondrial fragmentation. Over 70% of SA-treated and p53-silenced cells exhibited fragmented mitochondria that were absent in SA-treated only p53 WT cells (Figs 3B and 3C). Intriguingly, mitochondrial membrane potential (MMP) and levels of mitochondrial reactive oxygen species (ROS) were unaltered by increasing or decreasing the expression of p53 (Figs EV3E and EV3F). These results underscore the central role of p53 in the control of mitochondrial dynamics without affecting mitochondrial integrity.

Notably, single-cell tracking results showed that SA-treated cells exhibited a 1.5-fold decrease in migratory capacity as compared to that of control cells. Knockdown of p53 fully abolished the inhibitory effects of SA on cell migration. p53 silencing accelerated the migratory ability of SA-treated cells to a level similar to that of untreated and p53-depleted cells (Figs 3D and 3E). In line with this, transwell assays showed that SA lowered cell migration and invasion but these

effects were abolished by p53 silencing (Fig 3F). These results further support the suppressive role of p53 in the metastatic properties of cancer cells.

To further substantiate the role of p53 in regulating cell migration and invasion, we transfected the pcDNA3 p53 WT plasmid into the p53-null NSCLC H1299 cells to express exogenous WT p53 (Fig 3G). As monitored by wound-healing assays, expression of WT p53 caused an approximately 2.5-fold decrease in the migratory capacity of the cells as compared to that of the controls (Fig EV3G). Corroborating this finding, transwell assays also showed that expression of WT p53 significantly inhibited cell migration and invasion (Fig 3G). In conclusion, these results, together with the observation that p53 depletion exaggerated mitochondrial fragmentation and invasive cell migration, pinpoint p53 as a potent regulator of mitochondrial dynamics and cell motility.

p53 alleviates Drp1-mediated mitochondrial fission and thereby restrains cell migration and invasion

To delineate the underlying molecular mechanism responsible for enhanced mitochondrial fragmentation during p53 loss, we investigated changes in the expression and phosphorylation of mitochondrial fusion and fission factors in response to changes in p53 levels. Our qRT-PCR results showed that mRNA levels of mitochondrial fusion (Mfn1, Mfn2, and Opa1) and fission (Drp1, Fis1, Mff, and MIEF1) factors were unaltered upon p53 silencing in A549 cells (Fig EV4A). Additionally, both SA-induced p53 upregulation and siRNA-mediated p53 knockdown did not affect the protein levels of total Drp1 and Mfn2 (Fig 4A).

Phosphorylation of S616 on Drp1 enables Drp1-directed mitochondrial fission, whereas phosphorylation of S637 on the same protein abolishes its GTPase activity and inhibits the fission of mitochondria (Kraus & Ryan, 2017). While the levels of DRP1 S637 phosphorylation were unaffected by the expression levels of p53, SA-elevated p53 expression that caused

mitochondrial elongation (Figs 3B and 3C) triggered an ~50% reduction in the pro-fission S616 phosphorylation of Drp1 (Figs 4A and 4B). Conversely, in both untreated and SA-treated p53-silenced cells whose mitochondria were extensively fragmented (Figs 3B and 3C), Drp1 S616 phosphorylation was increased by over 4-fold when compared to that of the p53 WT controls (Figs 4A and 4B). These results suggest that p53 might control mitochondrial morphology by modulating the phosphorylation of S616 on Drp1.

Reportedly, mTORC1 phosphorylates 4EBPs to enable MTFP1 translation, thereby stimulating Drp1-mediated mitochondrial fission (Morita *et al.*, 2017). To illuminate how p53 controls Drp1 S616 phosphorylation, we examined the effects of p53 on the MTFP1 protein level and mTORC1 activity. In agreement with the Drp1 S616 phosphorylation and mitochondrial fission activity, the levels of MTFP1 and proteins relevant to mTORC1 signaling, including the phosphorylations of mTOR S2448, 4EBP1 S65, and S6K1 (p70 S6K) T389 were significantly decreased following SA-stimulated endogenous p53 expression in A549 cells. p53 depletion dramatically enhanced the MTFP1 protein level and mTORC1 activity in both untreated and SA-treated cells (Fig 4A). Furthermore, elevated p53 expression by SA also hampered the T202/Y204 phosphorylation of ERK1/2 (Fig 4A) whose activation was governed by Drp1-mediated mitochondrial fission (Sun *et al.*, 2018). p53 silencing, however, robustly augmented ERK1/2 phosphorylation in both untreated and SA-treated cells (Fig 4A).

To verify the regulation of mitochondrial dynamics and mTORC1 signaling by p53 is not restricted to A549 cells, we examined mitochondrial fission and fusion factors and mTORC1 signaling in MCF-7 (Fig 4C) and H1299 (Figs EV4B and EV4C) cells. Similar to findings in A549 cells, both SA-induced endogenous p53 upregulation and siRNA-mediated knockdown of p53 had no significant effect on the levels of Drp1, Mfn2, and Drp1 S637 phosphorylation in MCF-7 cells. Conversely, there was a robust increase in the S616 phosphorylation of Drp1, correlated with an elevation of MTFP1 protein levels and mTOR, 4EBP1, and S6K1 phosphorylations in

both untreated and SA-treated MCF-7 cells upon p53 silencing (Fig 4C). In sharp contrast to p53 WT A549 and MCF-7 cells, SA treatment did not affect the levels of Drp1, Mfn2, and Drp1 S637 phosphorylation, but it induced an ~2.5-fold increase in the levels of Drp1 S616 phosphorylation and a corresponding upregulation of MTFP1 protein levels and mTOR, 4EBP1, and S6K1 phosphorylations in p53-null H1299 cells (Figs EV4B and EV4C). Importantly, overexpression of exogenous WT p53 in control and SA-treated H1299 cells diminished Drp1 S616 phosphorylation by more than 40% and 50%, respectively, whereas levels of total Drp1, Mfn2, and Drp1 S637 phosphorylation were unaffected (Figs EV4B and EV4C). In line with this, phosphorylations of mTOR, 4EBP1, and S6K1 and the protein levels of MTFP1 were strongly decreased upon exogenous expression of WT p53 in both untreated and SA-treated H1299 cells (Fig EV4B). Altogether, these results support the notion that p53 drives mitochondrial elongation by inhibiting the phosphorylation of S616 on Drp1, accompanied by reducing MTFP1 protein levels and the mTORC1 activity.

The above discoveries prompted us to further investigate whether Drp1-mediated mitochondrial fission might contribute to the metastatic phenotype driven by p53 loss. To this end, we performed a double-knockdown of both p53 and Drp1 in A549 cells. In line with our conjecture that mTORC1-controlled MTFP1 protein translation is the upstream signaling that modulates Drp1 activity and mitochondrial fission (Morita *et al.*, 2017), co-knockdown of Drp1 in p53-silenced cells did not affect the total amounts and phosphorylations of mTOR, 4EBP1, and S6K1 and the protein levels of MTFP1 as compared to those in cells with p53 knockdown alone in either the absence or presence of SA (Fig 4A). In contrast, ERK1/2 phosphorylation was strongly reduced in cells with p53/Drp1 double-knockdown when compared to that in cells with p53 knockdown alone (Fig 4A), suggesting that ERK1/2 might be the downstream signaling regulated by Drp1-driven mitochondrial fission. Significantly, Drp1 depletion not only rescued p53 deficiency-induced mitochondrial fragmentation but also exaggerated mitochondrial

elongation. Over 80% and 90% of mitochondria were elongated in untreated and SA-treated p53/Drp1 double-knockdown cells, respectively (as compared to <1% in untreated and SA-treated p53-depleted cells) (Figs 4D and 4E). Most notably, Drp1 depletion abolished accelerated cell migration in untreated and SA-treated p53 knockdown cells, as illustrated by single-cell tracking (Figs EV4D and EV4E) and wound-healing assays (Figs EV4F). Consistently, transwell assays showed a more than 2-fold decrease in the migratory and invasive abilities of p53/Drp1 double-knockdown cells, when compared to those with only p53-knockdown (Fig 4F). Taken together, these results demonstrate that elevated mitochondrial fragmentation caused by increased Drp1 S616 phosphorylation is responsible for the aggressive cell migration and invasion seen upon p53 loss.

p53 diminishes mTORC1-controlled MTFP1 protein levels to attenuate Drp1-driven mitochondrial fission and invasive cell migration

Our results indicate that p53 silencing triggered mitochondrial fragmentation accompanied by an increase in Drp1 S616 phosphorylation and activation of mTORC1 signaling, whereas Drp1 depletion had no effect on the levels of mTORC1-relevant factors (Fig 4A). Possibly, mTORC1 functions upstream of Drp1 to drive Drp1 S616 phosphorylation and is inhibited by p53. To this end, we first examined the relationship between p53 and mTORC1. As expected, Pan-Cancer database analysis showed that p53 protein levels correlated inversely with 4EBP1 S65, 4EBP1 T37/T46, and mTOR S2448 phosphorylations (Fig 5A), suggesting a negative effect of p53 on mTORC1 activity. Since p53 acts predominantly as a transcription factor, we examined whether the transcriptional regulatory function of p53 is involved in the p53-driven suppression of mTORC1 activity and Drp1 S616 phosphorylation. Interestingly, the p53-specific transcriptional inhibitor, pifithrin-α (PFT-α), successfully suppressed the induction of the p53 downstream target p21 under the condition of SA-induced p53 upregulation. Furthermore, PFT-α did not affect p53 protein levels, but strongly enhanced mTOR, 4EBP1, and Drp1 S616

phosphorylations and the MTFP1 protein levels in both control and SA-treated A549 cells (Fig EV5A). These results are in line with the observations using p53 gene knockdown, suggesting that the transcriptional activity of p53 is essential for p53-mediated inhibition of mTORC1 and Drp1 activities. It has previously been illustrated that p53 stimulates the transcription of genes encoding negative regulators of mTOR signaling (Budanov & Karin, 2008; Feng *et al.*, 2007; Stambolic *et al.*, 2001; Vousden & Ryan, 2009). Accordingly, we found that p53 silencing attenuated the expression of those genes, including PTEN, AMPKβ1, Sestrin1/2, and TSC2 (Fig EV5B).

Increased or decreased p53 expression did not alter MTFP1 mRNA levels (Fig EV5C), suggesting that MTFP1 expression was controlled at the protein level. mTORC1 signaling reportedly mediates MTFP1 protein translation to govern Drp1 S616 phosphorylation and thereby mitochondrial fission (Morita *et al.*, 2017). To experimentally verify the interplay and chronology of mTORC1 signaling, MTFP1, and Drp1, we performed double knockdowns of p53 and mTOR or p53 and MTFP1 in A549 cells (Fig 5B). Knockdown of mTOR reduced the phosphorylations of mTORC1 downstream effectors 4EBP1 and S6K1 and diminished MTFP1 protein levels in both untreated and SA-treated p53-silenced A549 cells. In contrast, MTFP1 knockdown did not affect the total amounts and phosphorylations of mTORC1-relevant factors. The mTOR or MTFP1 silencing successfully abolished increased Drp1 S616 phosphorylation in both untreated and SA-treated p53 knockdown cells, while both mTOR and MTFP1 knockdown had no effect on total Drp1 and Mfn2 protein levels (Fig 5B). In line with the reduction of ERK1/2 activity seen upon Drp1 silencing (Fig 4A), ERK1/2 phosphorylation was dramatically diminished in both untreated and SA-treated p53/mTOR or p53/MTFP1 double-knockdown cells when compared with similar cells with only p53 silencing (Fig 5B). These results provide compelling evidence that mTORC1 mediating MTFP1 protein expression is required for the increased Drp1 S616 phosphorylation during p53 loss.

We further unraveled the contribution of the mTORC1/MTFP1 axis in modulating mitochondrial dynamics. Knockdown of either mTOR or MTFP1 completely rescued fragmented mitochondria in both untreated and SA-treated p53-depleted cells (Figs 5C and 5D). Mitochondria were elongated in ~90% of p53/mTOR or p53/MTFP1 double-knockdown cells untreated or treated with SA (Fig 5D). Consistent with the finding that mitochondrial dynamics impacts cell migration and invasion, exaggerated mitochondrial elongation triggered by mTOR or MTFP1 knockdown fully suppressed the migratory capacity of both untreated and SA-treated p53-depleted cells (Figs EV5D and EV5E). Transwell assays confirmed the dramatic reduction of both migratory and invasive abilities in p53/mTOR or p53/MTFP1 double-knockdown cells as compared to those in cells with p53 silenced alone (Fig 5E). In conclusion, these results demonstrate that the control of MTFP1 protein levels by mTORC1 signaling is critical for p53 deficiency-induced mitochondrial fragmentation and accelerated cell migration and invasion.

Activation of mTORC1/MTFP1/Drp1/ERK signaling axis is required for increased MMP9 expression and cancer dissemination upon WT p53 loss

Building on our findings that p53 silencing elevated ERK1/2 phosphorylation but could be counteracted by co-knockdown of Drp1, mTOR, or MTFP1 (Figs 4A and 5B), we theorized that mitochondrial fission governed by mTORC1/MTFP1/Drp1 axis might activate ERK1/2 signaling to direct cell migration and invasion upon p53 loss. Indeed, we observed that ERK1/2 phosphorylation displayed inverse and direct correlations with p53 and the phosphorylations of mTORC1-relevant factors (mTOR and 4EBP1), respectively (Fig 6A). Inhibition of ERK1/2 with PD98059 had no significant effect on the MTFP1 protein levels and the phosphorylations of Drp1 and 4EBP1 in p53-silenced cells with and without SA-treatment (Fig 6B). In contrast, similar to observations seen upon depletion of Drp1, mTOR, or MTFP1, inhibition of ERK1/2 rescued the aggressive cell phenotype caused by p53 silencing (Fig EV6A). ERK1/2 inhibition also hampered p53 deficiency-accelerated cell motility and invasion (Figs 6C, EV6B, and

EV6C). Thus, ERK1/2 signaling functions downstream of mitochondria whose morphology is modulated by the mTORC1/MTFP1/Drp1 axis to favor cell dissemination upon p53 loss.

Finally, we sought to identify the metastasis-associated gene expression signature involved in exaggerated cell migration and invasion directed by the mTORC1/MTFP1/Drp1/ERK axis following p53 loss. Several studies have highlighted that ERK1/2 activation stimulates the expression of MMP9, which contributes to the proteolytic degradation of the extracellular matrix (Lakka *et al*, 2002; Li *et al*, 2018; Wang *et al*, 2017a; Yao *et al*, 2001). Strikingly, we observed elevated levels of MMP9 gene expression in p53-silenced A549 (Fig 6D) and MCF-7 (Fig EV6D) cells when compared to those in p53 WT cells. Inhibition of ERK1/2 activation completely abolished the increased MMP9 expression in p53-depleted cells. In line with this, co-knockdown of Drp1, mTOR, or MTFP1 in p53-silenced cells restored MMP9 expression to levels similar to the controls (Figs 6D and EV6D). Moreover, the levels of MMP9 mRNA were lower in cancer patients harboring WT *TP53* than in those with MUT *TP53* (Fig 6E). The protein levels of p53 also exerted a negative correlation with the mRNA levels of MMP9 in cancers having WT *TP53* (Fig 6F).

Consistent with previous literature showing that increased MMP9 expression promotes cancer cell migration, invasion, and metastasis (Quintero-Fabián *et al*, 2019), MMP9 mRNA levels were enhanced in N1+ (Fig 6G) and advanced-stage (III and IV) (Fig 6H) tumors when compared to those in N0 and the earlier-stage (I and II) tumors, respectively. MMP9 mRNA levels were also higher in metastatic than in primary melanoma (Fig EV6E). Higher MMP9 levels were associated with worse overall survival in cancer patients (Fig 6I, left). The median overall survival was 86.14 and 93.20 months in patients expressing high and low MMP9 mRNA levels, respectively. Of cancer patients harboring WT *TP53*, those with high MMP9 mRNA and low p53 protein expression showed a significantly increased risk of death when compared to those with low MMP9 mRNA and high p53 protein expression (the median overall survival was 112.1 and

146.1 months, respectively) (Fig 6I, right). Collectively, these results suggest that in p53-silenced cells, the mTORC1/MTFP1/Drp1/ERK axis might induce MMP9 expression to accelerate the metastatic dissemination of cancer cells and confirm the clinical implications for MMP9 in cancers.

Discussion

This study unravels a molecular explanation of how tumor suppressor p53 modulates mitochondrial dynamics to restrict cancer cell dissemination. For the first time, we link p53 to mitochondria-dependent regulation of malignant properties of cancers, including cell motility and metastasis. p53 is canonically known to suppress cancer development by regulating multiple cell fate-determining genes involved in cell cycle arrest, DNA damage repair, senescence, and apoptosis (Kastenhuber & Lowe, 2017). p53 also constrains the metastatic abilities of cancer cells by transcriptionally controlling components of the metastatic cascade (Powell *et al.*, 2014). We present evidence here that p53 suppresses cancer dissemination via mitochondrial dynamics modulation and provide an alternative mechanism that coordinates aggressive phenotypes in cancers harboring compromised p53. The strong positive correlation between p53 expression levels and overall survival in cancer patients may be at least in part resulted from its anti-metastatic effects.

mTORC1 is commonly hyper-activated in p53-compromised cancers (Kong *et al*, 2015) and contributes to cancer cell migration (Harvey *et al.*, 2019; Liu *et al.*, 2006). However, the underlying molecular signaling pathways remain poorly understood. We show here that mTORC1 accelerates cancer dissemination by directing MTFP1 protein expression. MTFP1 then facilitates Drp1-mediated mitochondrial fission upon p53 loss. These findings provide an important insight into a hitherto unknown mechanism that links mTORC1 to cancer metastasis.

Recently, MTFP1 has also been implicated in promoting MMP9 expression and cancer metastasis although the underlying mechanism is still unknown (Zhang *et al*, 2018). Our results further corroborate the pro-migratory functions of MTFP1 and for the first time provide a molecular explanation for the observations. Accordingly, MTFP1 facilitates Drp1-mediated mitochondrial fission to enable ERK1/2 activation, thereby triggering the EMT-associated morphologic switch accompanied by exaggerated MMP9 expression and cancer cell dissemination. This underscores components of the mTORC1/MTFP1/Drp1/ERK signaling as potential and effective therapeutic targets for treating malignant and metastatic p53-compromised tumors (de la Cruz López *et al*, 2019; Zhang *et al*, 2019).

It is interesting to note that enhanced mitochondrial fragmentation is not always due to the accumulation of damaged mitochondria. Instead, mitochondrial biogenesis, by which new functional mitochondria are generated, also requires the initiation of Drp1-driven mitochondrial fission (Kleele *et al*, 2021; Kraus *et al*, 2021; Popov, 2020). Fissions derived from mitochondrial dysfunction are associated with increased mitochondrial ROS and diminished MMP (Burman *et al*, 2017; Kleele *et al.*, 2021; Twig *et al*, 2008), whereas the mitochondrial physiology during fissions in the biogenesis of new mitochondria remains unchanged (Kleele *et al.*, 2021). Intriguingly, our data show that depletion of p53 exaggerates mitochondrial fragmentation, but it does not affect MMP and mitochondrial ROS levels. In addition, it has been reported that mitochondrial biogenesis is regulated by the mTORC1/4EBP pathway which stimulates the translation of mRNAs encoding mitochondria-related proteins (Morita *et al.*, 2013). Here, we show that p53 depletion activates mTORC1/4EBP1 signaling that regulates MTFP1 protein expression to govern Drp1-mediated mitochondrial fission. Thus, we speculate that increased mitochondrial fission upon p53 loss is associated with stimulation of mitochondrial biogenesis, but not accumulation of damaged mitochondria. This would explain how the mitochondrial

physiology remains constant in the context of p53 deficiency-induced mitochondrial fragmentation.

Accumulating evidence illustrates the critical roles of intracellular calcium (Ca^{2+}) signaling in the regulation of key steps of the metastatic cascade, including EMT, focal adhesion turnover, lamellipodia formation, and the degradation of the extracellular matrix (Prevarskaya *et al*, 2011; Tsai *et al*, 2014; White, 2017). Notably, mitochondrial fission reduces the potential of endoplasmic reticulum (ER)-mitochondrial contacts and thereby attenuates the capacity of mitochondria to sequester Ca^{2+} released from the ER, leading to an increase in cytosolic Ca^{2+} levels (Maltecca *et al*, 2012; Wang *et al*, 2017b). Moreover, mitochondrial fission resulting in elevated Ca^{2+} levels in the cytoplasm activates multiple Ca^{2+}-dependent pathways regulating cellular behaviors, including cell migration and invasion (Huang *et al*, 2017; Ponte *et al*, 2020; Sun *et al.*, 2018). Consistently, we find that exaggerated mitochondrial fission upon p53 loss triggers increased phosphorylation of ERK1/2, which is a downstream target of Ca^{2+}/calmodulin-dependent protein kinase II (CaMKII), a major decoder of the intracellular Ca^{2+} oscillations (Illario *et al*, 2003; Sun *et al.*, 2018). Intriguingly, pharmacological inhibition of ERK1/2 activity highlights an indispensable role of ERK1/2 signaling in controlling cell morphology, MMP9 expression, and cancer cell dissemination upon p53 loss. Our observations are supported by studies indicating that ERK1/2 stimulates MMP9 expression via regulating the activity of the transcription factors NF-κB (nuclear factor kappa-light-chain-enhancer of activated B cells) and AP-1 (activator protein-1) (Lakka *et al.*, 2002; Lin *et al*, 2015; Moon *et al*, 2004). Furthermore, the ERK1/2 signaling is implicated in controlling numerous other components of the cell motility machinery (Hino *et al*, 2020; Tanimura & Takeda, 2017). For example, ERK1/2 signaling promotes cancer cell migration, invasion, and EMT by mediating the expression or the transcriptional activity of EMT-inducing transcription factors Twist1 (Hong *et al*, 2011; Weiss *et al*, 2012), Snail (Li *et al*, 2017; Nagarajan *et al*, 2012), and Slug (Virtakoivu *et al*, 2015). Thus,

specific ERK1/2 inhibition may be beneficial to slow cancer metastasis in patients harboring compromised p53.

In summary, we have illustrated how p53 can modulate mitochondrial dynamics via controlling the mTORC1/MTFP1/Drp1 axis to restrict cancer cell dissemination (Fig 7). Accordingly, cells with WT p53 exhibit basal mTORC1 activity, basal MTFP1 protein levels, and a coordinated balance between mitochondrial fission and fusion events. This maintains the mitochondrial morphology in a predominantly intermediate state and thereby prevents ERK1/2-governed cell migration and invasion. Cells with p53 silenced have increased activity of mTORC1 and the corresponding augmented MTFP1 protein levels. MTFP1 favors the pro-fission S616 phosphorylation of Drp1, which subsequently activates ERK1/2 signaling to enable EMT-associated morphological changes, MMP9 expression, and invasive cell migration. The molecular mechanism uncovered in this study is likely a general phenomenon. Indeed, we could observe the downregulation of WT p53 and the elevations of the pro-fission factor Drp1 and the metastatic driver MMP9 in aggressive and malignant tumors across cancers in The Cancer Genome Atlas. Additionally, Pan-Cancer analysis also showed that reduced WT p53 expression and enhanced expression of Drp1 or MMP9 are strongly correlated with poor prognosis. Our results offer a new molecular explanation for the aggressive malignant phenotypes of p53-compromised cancers and are highly beneficial to the discovery of novel therapeutic approaches nullifying pro-metastatic signals regulated by mitochondrial dynamics upon loss of WT p53 functions.

Materials and Methods

Cell lines and cell culture conditions

A549 and H1299 cells were maintained in Roswell Park Memorial Institute (RPMI) 1640 medium supplemented with 10% heat-inactivated fetal bovine serum (FBS), 0.22% sodium bicarbonate, 2 mM L-glutamine (L-Gln), and 100 units/ml penicillin/streptomycin (P/S). MCF-7 cells were maintained in Dulbecco's modified Eagle's medium (DMEM) containing 10% FBS, 0.37% sodium bicarbonate, 2 mM L-Gln, and 100 units/ml P/S. All cells were cultured at 37 °C in a humidified incubator supplemented with 5% CO_2.

Reagents and treatments

Reagents for cell cultures were purchased from Invitrogen Gibco (Grand Island, NY, USA). Other chemicals in this study were purchased from Sigma-Aldrich (St. Louis, MO, USA) unless specified. Sodium arsenite was obtained from Merck (Darmstadt, Germany). MTT (3-(4,5-dimethylthiazol-2-yl-2, 5-diphenyl tetrazolium bromide)) was purchased from Alfa Aesar (Thermo Fisher Scientific, Leicestershire, UK). MitoTracker Green FM, MitoSOX Red, JC-1 dye, TRIzol reagent, reagents for reverse transcription and transfection, and siRNAs were purchased from Invitrogen (Carlsbad, CA, USA). Matrigel basement membrane matrix was purchased from Corning (Tewksbury, MA, USA). Primers used in qRT-PCR were purchased from Integrated DNA Technologies (Coralville, IA, USA). PD98059 was purchased from Enzo Life Sciences (Farmingdale, NY, USA).

Sodium arsenite (SA) (Merck) was dissolved in deionized water and added to culture medium at indicated concentrations (10, 20, 40, and 80 μM) for 24 h. Pifithrin-α (PFT-α) (Sigma-Aldrich) and PD98059 (Enzo Life Sciences) were dissolved in dimethyl sulfoxide (DMSO) (Sigma-

Aldrich). Cells were pretreated with PFT-α or PD98059 at 20 μM for 3 h or 30 μM for 2 h, respectively, prior to treatment with 20 μM SA for 24 h.

siRNA and plasmid transfection

Small interference (si)RNA-mediated gene knockdown experiments were carried out with cells transfected with 10 nM siRNA (Invitrogen) for 3 days using Lipofectamine RNAimax (Invitrogen) following the manufacturer's reverse transfection instructions. A Stealth RNAi siRNA Negative Control (Invitrogen) was used as control. See table EV1 for information about siRNA target sequences.

The pcDNA3 p53 WT plasmid was constructed by inserting a WT p53 gene (393 amino acids) into a pcDNA3 plasmid. Transient expression of WT p53 in H1299 cells was carried out by transfecting cells with the pcDNA3 p53 WT plasmids for 2 days using Lipofectamine 2000 reagent (Invitrogen) according to the manufacturer's protocol. An empty pcDNA3 plasmid was used as control.

Cell lysis, immunoblotting, and antibodies

Cells were harvested by trypsinization and centrifugation at 700 × *g* for 5 min at 4 °C and lysed in ice-cold radioimmunoprecipitation assay (RIPA) lysis buffer (50 mM Tris-HCl (pH8.0), 150 mM NaCl, 5 mM EDTA (pH 8.0), 1% NP-40, 0.1% SDS, and 0.5% sodium deoxycholate) supplemented with complete protease and phosphatase inhibitor cocktails (Fivephoton Biochemicals, San Diego, CA, USA). Cell suspension was subsequently incubated on ice for 10 min and then vortexed vigorously for 5 sec. The incubation and vortexing steps were repeated four times, and cell lysates were separated from debris by centrifugation at 12,000 × *g* for 20 min at 4 °C. After centrifugation, the supernatants were transferred to new tubes and protein concentrations were determined using the Bio-Rad protein assay (Bio-Rad, Hercules, CA, USA). Proteins in cell lysates were separated on SDS-PAGE and then transferred

electrophoretically onto PVDF membranes (GE Healthcare, Milwaukee, WI, USA) using a transfer cell (Bio-Rad, Hercules, CA, USA). Membranes were subsequently pre-hybridized in TBST buffer (150 mM NaCl, 10 mM Tris-HCl (pH 8.0), 0.1% Tween-20) with 5% skim milk for 1 h before incubating overnight with appropriate primary antibodies diluted in TBST buffer containing 5% bovine serum albumin (BSA). Antibodies against p53 (GTX70214) and GAPDH (GTX100118) were purchased from GeneTex (Hsinchu, Taiwan). Antibodies against Drp1 (8570), phospho-Drp1 (Ser616) (3455), phospho-Drp1 (Ser637) (4867), Mfn2 (11925), 4EBP1 (9644), phospho-4EBP1 (Ser65) (9456), p70 S6K (2708), phospho-p70 S6K (Thr389) (9234), mTOR (2972), phospho-mTOR (Ser2448) (2971), ERK1/2 (9102), and phospho-ERK1/2 (Thr202/Tyr204) (4370) were purchase from Cell Signaling Technology (Beverly, MA, USA). Antibodies against MTFP1 (ab198217) were from Abcam (Cambridge, UK). Antibodies against Caspase-2 (MAB3507) and MDM2 (MABE340) were from EMD Millipore Corporation (Burlington, NC, USA). All antibodies were used at a 1:1000 dilution except anti-GAPDH (1:10,000 dilution) and anti-MTFP1 (1:500 dilution).

After primary antibody incubation, membranes were washed three times for 15 min each with TBST buffer, then incubated for 1 h with the respective horseradish peroxidase (HRP)-conjugated secondary antibodies diluted to 5000 folds in TBST buffer containing 5% skim milk. HRP-conjugated anti-rabbit IgG (NA934V) and anti-mouse IgG (NA931V) were from Amersham (GE Healthcare, Buckinghamshire, UK). HRP-conjugated rabbit anti-rat IgG (ab6734) was from Abcam (Cambridge, UK). Membranes were then washed three times for 15 min each with TBST buffer and detected by chemiluminescence using CyECL Western Blotting Substrate H (Cyrusbioscience, MDBio, Taipei, Taiwan).

Visualization was processed with an ImageQuant LAS 4000 mini biomolecular imager (GE Healthcare), and the intensities of bands were quantified with the UN-SCAN-IT gel analysis software (version 6.1) (Silk Scientific, Orem, UT, USA). Signal intensities of total proteins were

normalized to GAPDH. Signal intensities of phosphorylated proteins were calculated by dividing the GAPDH-normalized signal intensity for each phosphorylated protein by the GAPDH-normalized intensity of the corresponding total protein.

Live single-cell tracking

The single-cell motility assay was performed as described previously (Kuo *et al*, 2020). Briefly, 1×10^4 cells were plated in 6-well cell culture plates (Corning) and incubated in 5% CO_2 at 37 °C. Time-lapse microscopy was performed using an LS620 Microscope (Lumascope, San Diego, CA, USA). Live-cell images were taken automatically every 10 min over a 24 h period. Single-cell migration distance and trajectory were analyzed at two different X-Y positions using the "Manual Tracking" plugin of the ImageJ software (NIH, Bethesda, MD, USA).

***In vitro* wound-healing assay**

The scratch wound-healing assay was performed as previously described (Liang *et al*, 2007). Briefly, cells were grown to confluence in 6-well cell culture plates (Corning). A linear wound was created by scratching the cell monolayer with a sterile p200 pipette tip. Cells were washed several times before incubating in an FBS-free medium. To monitor the migration of cells back into the wound area, cells were imaged at 0 h and 24 h after scratching using a Dino-Eye Microscope Eyepiece Camera (AnMo Electronics Corporation, New Taipei City, Taiwan) connected to a Nikon TMS-F Inverted Phase Contrast Microscope (Nikon, Tokyo, Japan). The area of the wound was quantified by the "Wound Healing Tool" plugin of the ImageJ software (NIH, Bethesda, MD, USA). The relative migration into the wound was calculated by normalizing the measured wound closure area to the area of the initial wound at the 0 h time point.

Transwell cell migration and invasion assays

Transwell cell migration assays were performed using 24-well cell culture inserts with an 8.0-μm pore size transparent polyethylene terephthalate (PET) membrane (Corning) according to the manufacturer's recommendations. Briefly, 2.5 × 10^5 cells in 200 μl of serum-free medium were loaded into the upper chamber of each insert. The bottom wells were filled with 750 μl of complete medium containing 10% FBS. The cells were cultured in a humidified incubator at 37 °C supplemented with 5% CO_2. After 16 h, nonmigratory cells on the upper surface of the inserts were carefully removed with cotton swabs. Migrated cells attached to the lower surface of the inserts were fixed with 4% paraformaldehyde (PFA) (Electron Microscopy Sciences, Hatfield, PA, USA) for 2 min, permeabilized with 100% methanol for 20 min, then stained with 0.05% crystal violet (Sigma-Aldrich) for 15 min at room temperature. Migrated cells were observed and imaged using a Dino-Eye Microscope Eyepiece Camera (AnMo Electronics Corporation, New Taipei City, Taiwan) connected to a Nikon TMS-F Inverted Phase Contrast Microscope (Nikon, Tokyo, Japan). The bound crystal violet was eluted with 33% acetic acid (Mallinckrodt Chemicals, Phillipsburg, NJ, USA) and quantified by measuring the absorbance at 595 nm with a microplate reader (Bio-Rad, Hercules, CA, USA). The relative ability of migration was calculated as folds changed in absorbance of the indicated sample in relation to the control. In the invasion assay, 5 × 10^5 cells were plated onto the Matrigel-coated inserts and the same procedure as described above was followed.

Live-cell fluorescence microscopy and quantification of mitochondrial morphology

1×10^4 A549 cells were grown in poly(D-lysine)-coated borosilicate glass Lab-Tek 8-well chambers (Thermo Scientific) and stained with MitoTracker Green FM (Invitrogen) (50 nM) for 30 min. After staining, cells were washed three times in prewarmed PBS and replaced with fresh prewarmed medium. Live-cell fluorescence images were acquired on a Nikon Eclipse Ti inverted microscope with a 60X oil objective lens (Nikon) and DS-Qi2 CMOS camera (Nikon) using Nikon element AR software (Nikon). Fluorescence images with 15 stacks of 0.3 μm each

were deconvoluted using Huygens Essential Software (Scientific Volume Imaging, Hilversum, North Holland, Netherlands). The maximum intensity projections of images were generated by Nikon element AR software (Nikon). Images were mainly processed and analyzed using Nikon element AR software (Nikon) and mitochondrial morphology was classified as elongated, intermediate, or fragmented. Elongated mitochondria were those that have long tubulating or spreading reticular networks. Cells displaying mitochondria that are small spherical, ovoid, or short rod-shaped were presented as fragmented. Cells containing a mixture of small spherical and shorter tubular mitochondria were classified as intermediate.

Cell viability assay

Cells were seeded in 96-well cell culture plates (TPP Techno Plastic Products AG, Trasadingen, Switzerland) at a density of 4×10^3 cells per wells. Cell viability was assessed using MTT assay (Thermo Fisher Scientific) according to the manufacturer's instructions. Cells were added with 0.4 mg/ml of MTT reagent and incubated for 4 h at 37 °C before the absorbance at 550 nm was measured with a microtiter plate reader (Bio-Rad).

Colony formation assay

1×10^3 cells were seeded in 6-well plates (Corning) and incubated with complete medium at 37 °C in 5% CO_2 for 24 h to facilitate their attachment. Subsequently, cells were treated with various concentrations of sodium arsenite for an additional 24 h period before the medium was removed and replaced with the fresh medium containing 10% FBS. After 14 days of incubation, cells were fixed in 4% PFA (Electron Microscopy Sciences) for 20 min and stained with 0.05% crystal violet (Sigma-Aldrich) for 2 h. Colonies were imaged and measured by the ImageJ software (NIH, Bethesda, MD, USA).

Flow cytometry

All experiments were performed using 6-well plates (Corning). A total of 10,000 events, excluding debris, were recorded for each sample. All flow cytometric data were obtained using BD Accuri C6 flow cytometer (BD Biosciences, San Jose, CA, USA) and analyzed by the FlowJo 7.6.1 software (FlowJo LLC, Ashland, OR, USA).

For measurement of mitochondrial membrane potential (MMP) and mitochondrial reactive oxygen species (ROS), cells were treated with trypsin and prepared as single-cell suspensions. Cells were then stained either with 2 µM of the MMP probe JC-1 (Invitrogen) for 20 min or with 5 µM of the mitochondrial superoxide indicator MitoSOX Red (Invitrogen) for 30 min following the manufacturer's protocols. Cells were washed twice in ice-cold PBS before analysis with flow cytometry.

RNA isolation and quantitative real-time PCR (qRT-PCR)

Total RNA was extracted using TRIzol reagent (Invitrogen) following the procedures provided by the manufacturer. The extracted RNA was reverse-transcribed with a RevertAid First Strand cDNA Synthesis Kit (Invitrogen). The resulting complementary (c)DNA was used for quantitative real-time PCR (qRT-PCR) using SYBR Green PCR Master Mix (Applied Biosystems, Foster City, CA, USA) on a StepOnePlus Real-Time PCR system (Applied Biosystems). Data were acquired and analyzed using StepOne Software v2.3 (Thermo Fisher Scientific). The expression of glyceraldehyde 3-phosphate dehydrogenase (GAPDH) was determined in each sample and used as reference gene. Expression of target genes was compared on the basis of equivalent GAPDH transcripts using the $2^{-\Delta\Delta Ct}$ method. See table EV2 for information about primer sequences.

***TP53* gene statuses and clinical correlations**

Data of *TP53* gene statuses (WT and MUT *TP53*) used to analyze the associations between the presence of TP53 mutations and the probabilities of metastases to lymph nodes (Fig 1A) and

distant organs (Fig 1B) were derived from the TCGA Pan-Cancer and the Memorial Sloan-Kettering Integrated Mutation Profiling of Actionable Cancer Targets (MSK-IMPACT) (Zehir *et al*, 2017) cohorts respectively, downloaded from the cBioPortal for Cancer Genomics (https://www.cbioportal.org/) (Cerami *et al*, 2012; Gao *et al*, 2013). In each dataset, tumors were stratified into one of two categories: tumors with no *TP53* alteration (WT *TP53*), or tumors with one or more *TP53* mutations (MUT *TP53*). The complete TCGA Pan-Cancer dataset includes a total of 10,967 tumors from 10,953 patients across 32 different cancer types. *TP53* mutation data are available from 10,960 tumors. Among these tumor samples, 6528 tumors have data of lymph node metastatic status (Fig 1A) and 10,813 tumors have data of overall survival (Fig 1C). The complete MSK-IMPACT cohort includes 10,945 tumors from 10,336 patients having both data of *TP53* mutations and tumor sites (Fig 1B). The significance of the associations between the presence of TP53 mutations and the probabilities of metastases to lymph nodes (Fig 1A) and distant organs (Fig 1B) was determined by Fisher's exact test. The significance of the difference in the Kaplan-Meier plot of the overall survival in patients with WT and MUT *TP53* (Fig 1C) was determined by log-rank (Mantel-Cox) test.

Differential protein expression analysis

Comparative analyzes of p53 protein expression levels (Figs 1D and 1E) were performed using the reverse-phase protein array (RPPA) data acquired from the TCGA Pan-Cancer dataset in the cBioPortal for Cancer Genomics (https://www.cbioportal.org/) (Cerami *et al.*, 2012; Gao *et al.*, 2013). A total of 4741 tumors harboring WT *TP53* and having RPPA data were retrieved. Of which, 2934 tumors have data of lymph node metastatic status (Fig 1D) and 3086 tumors have data of disease stages (Fig 1E). RPPA values for p53 expression levels were stratified according to the lymph node metastatic status and the stage of the corresponding patient tumor. Mean protein expression levels of p53 were determined in lymph node-negative (N0) and -positive (N1+) (Fig 1D) or earlier-stage (stage I+II) and advanced-stage (stage III+IV) (Fig 1E)

groups and significant downregulation of p53 protein expression in N1+ and advanced-stage tumors were statistically analyzed by two-tailed Student's t test (unpaired).

Differential gene expression analysis

Comparative analysis of gene expression patterns of p53 (Fig EV1A), Drp1 (Fig EV2A), and MMP9 (Fig EV6E) between primary and metastatic melanoma was performed using the RNA-Seq by Expectation-Maximization (RSEM) data extracted from TCGA in The UCSC Xena Browser (http://xena.ucsc.edu/) (Goldman *et al*, 2020). Pan-Cancer analyzes of the differential gene expression of Drp1 (Figs 2C and 2D) and MMP9 (Figs 6G and 6H) among tumor samples obtained from patients with lymph node-negative (N0) and -positive (N1+) prognostics (Figs 2C and 6G) or at different stages (stage I+II and III+IV) (Figs 2D and 6H); and that of EMT drivers Twist1, Slug, Snail (Fig EV1E), and MMP9 (Fig 6E) among tumor samples with WT and MUT *TP53* were performed using RSEM values acquired from the TCGA Pan-Cancer dataset in the cBioPortal for Cancer Genomics (https://www.cbioportal.org/) (Cerami *et al.*, 2012; Gao *et al.*, 2013). RSEM data are available for 10,071 tumors. Of these tumors, 6445 tumors have data of lymph node metastatic status (Figs 2C and 6G), 6613 tumors have data of cancer stages (Figs 2D and 6H), and 10,070 tumors have data of *TP53* mutation status (Figs EV1E and 6E).

All RSEM values were log2 transformed. Similar to methods used for protein expression data, mean expression levels were determined for mRNAs in individual groups and significant up- or down-regulation of mRNA expression was statistically analyzed by two-tailed Student's t test (unpaired).

Correlation analysis

The correlations between protein expression levels of p53 versus mRNA expression levels of Twist1 (Fig EV1B), Slug (Fig EV1C), Snail (Fig EV1D), and MMP9 (Fig 6F); or mRNA expression levels of Drp1 versus those of Twist1 (Fig EV2B) and Slug (Fig EV2C) were

determined using RPPA and RSEM values extracted from the TCGA Pan-Cancer dataset in the cBioPortal for Cancer Genomics (https://www.cbioportal.org/) (Cerami *et al.*, 2012; Gao *et al.*, 2013). All RSEM values were log2 transformed. Of the 10,071 tumors with available RSEM data (Figs EV2B and EV2C), 4538 tumors harbor WT *TP53* and have RPPA data (Figs EV1B-D and 6F).

For the correlations between p53 protein expression levels versus 4EBP1 S65, 4EBP1 T37/T46, and mTOR S2448 phosphorylation levels (Fig 5A); or ERK1/2 T202/Y204 phosphorylation levels versus p53 protein levels and phosphorylation levels of 4EBP1 S65, 4EBP1 T37/T46, and mTOR S2448 (Fig 6A), we used level 4 normalized RPPA data of the TCGA Pan-Cancer cohort downloaded from The Cancer Proteome Atlas (https://tcpaportal.org/). The Pearson correlation coefficient (r) was used to establish the correlations between expression levels of proteins versus mRNAs, proteins versus proteins, and mRNAs versus mRNAs and determine the *p-value*.

Survival analysis

For correlation analysis of p53 protein expression levels and the overall survival of cancer patients harboring WT *TP53* (Fig 1F), publicly available RPPA data and patients' overall survival status from the TCGA Pan-Cancer dataset were downloaded from the cBioPortal for Cancer Genomics (https://www.cbioportal.org/) (Cerami *et al.*, 2012; Gao *et al.*, 2013). Of tumors with WT *TP53*, 4700 tumors have both RPPA and overall survival data. Patients were split into high and low p53 expression groups based on the median values of p53 protein expression. The significance of the difference in the overall survival of patients with high and low p53 protein expression in Kaplan-Meier plots was determined by log-rank (Mantel-Cox) test.

For correlation analysis of mRNA expression levels of Drp1 (Fig 2E) and MMP9 (Fig 6I) versus overall survival of cancer patients, RSEM values and patients' overall survival data from the

TCGA Pan-Cancer dataset were downloaded from the cBioPortal for Cancer Genomics (https://www.cbioportal.org/) (Cerami *et al.*, 2012; Gao *et al.*, 2013). A total of 9994 tumors having both RSEM and overall survival data were retrieved. Similar to methods used for the analysis of correlation of p53 protein expression patterns and overall survival, patients were split into high and low expression groups based on the median values of Drp1 and MMP9 mRNA expression. The significance of the difference in the overall survival of patients with high and low expressions of individual mRNAs in Kaplan-Meier plots was determined by log-rank (Mantel-Cox) test.

Software and statistical analysis

All analyzes of clinical data carried out in this paper are based upon data generated by The Cancer Genome Atlas (TCGA) Research Network (https://www.cancer.gov/tcga) except the association between the presence of TP53 mutations versus the probability of distant metastasis (MSK-IMPACT cohort) (Fig 1B). Data were presented as means ± SD or SEM of at least three independent experiments. All graphing and statistical analyses were performed using GraphPad Prism 7 software. Details of sample size (n), statistical test, and *p-value* applied for each experiment were indicated in the figure legends. Values with $p < 0.05$ and designated with * are considered statistically significant. All composite figures were assembled in Adobe Illustrator.

Data availability

This paper analyzes existing, publicly available data and does not generate any unique datasets.

Acknowledgments

We thank Dr. Ming F. Tam (Department of Biological Sciences, Carnegie Mellon University, Pittsburgh, PA, USA) for the critical reading of the manuscript. This work was supported by grants 107-2514-S-007-001 (L.-Y.L), 109-2636-B-007-003 and 108-26 (Y.-C.L.), and 109-2320-B-007 -003 -MY3 (Y.-T.C) from the Ministry of Science and Technology, Taiwan.

Author contributions

Conceptualization, L.-Y.L. and T.T.T.P.; Methodology, L.-Y.L., T.T.T.P., Y.-C.L., Y.-T.C., and C.-W.W; Data Analysis and Curation, T.T.T.P. and L.-Y.L., and Y.-C.L.; Investigation, T.T.T.P., L.-Y.L., Y.-C.L., and Y.-T.C.; Resources, L.-Y.L., Y.-C.L., and Y.-T.C.; Writing – Original Draft, T.T.T.P. and L.-Y.L.; Writing – Review & Editing, L.-Y.L., T.T.T.P., Y.-T.C., and Y.-C.L.; Visualization, T.T.T.P. and L.-Y.L.; Supervision, L.-Y.L.; Project Administration, L.-Y.L.; Funding Acquisition, L.-Y.L, Y.-C.L., and Y.-T.C.

Declaration of interests

The authors declare no competing interests.

References

Achanta G, Sasaki R, Feng L, Carew JS, Lu W, Pelicano H, Keating MJ, Huang P (2005) Novel role of p53 in maintaining mitochondrial genetic stability through interaction with DNA Pol γ. *The EMBO Journal* 24: 3482-3492

Budanov AV, Karin M (2008) p53 Target Genes Sestrin1 and Sestrin2 Connect Genotoxic Stress and mTOR Signaling. *Cell* 134: 451-460

Burman JL, Pickles S, Wang C, Sekine S, Vargas JNS, Zhang Z, Youle AM, Nezich CL, Wu X, Hammer JA *et al* (2017) Mitochondrial fission facilitates the selective mitophagy of protein aggregates. *Journal of Cell Biology* 216: 3231-3247

Caino MC, Seo JH, Aguinaldo A, Wait E, Bryant KG, Kossenkov AV, Hayden JE, Vaira V, Morotti A, Ferrero S *et al* (2016) A neuronal network of mitochondrial dynamics regulates metastasis. *Nature Communications* 7: 13730

Cerami E, Gao J, Dogrusoz U, Gross BE, Sumer SO, Aksoy BA, Jacobsen A, Byrne CJ, Heuer ML, Larsson E *et al* (2012) The cBio Cancer Genomics Portal: An Open Platform for Exploring Multidimensional Cancer Genomics Data. *Cancer Discovery* 2: 401-404

de la Cruz López KG, Toledo Guzmán ME, Sánchez EO, García Carrancá A (2019) mTORC1 as a Regulator of Mitochondrial Functions and a Therapeutic Target in Cancer. *Frontiers in Oncology* 9

Fares J, Fares MY, Khachfe HH, Salhab HA, Fares Y (2020) Molecular principles of metastasis: a hallmark of cancer revisited. *Signal Transduct Target Ther* 5: 28

Feng Z, Hu W, de Stanchina E, Teresky AK, Jin S, Lowe S, Levine AJ (2007) The Regulation of AMPK β1, TSC2, and PTEN Expression by p53: Stress, Cell and Tissue Specificity, and the Role of These Gene Products in Modulating the IGF-1-AKT-mTOR Pathways. *Cancer Research* 67: 3043-3053

Gao J, Aksoy BA, Dogrusoz U, Dresdner G, Gross B, Sumer SO, Sun Y, Jacobsen A, Sinha R, Larsson E *et al* (2013) Integrative Analysis of Complex Cancer Genomics and Clinical Profiles Using the cBioPortal. *Science Signaling* 6: pl1-pl1

1 Giorgi C, Marchi S, Pinton P (2018) The machineries, regulation and cellular functions of
2 mitochondrial calcium. *Nat Rev Mol Cell Biol* 19: 713-730

3 Goldman MJ, Craft B, Hastie M, Repečka K, McDade F, Kamath A, Banerjee A, Luo Y, Rogers
4 D, Brooks AN *et al* (2020) Visualizing and interpreting cancer genomics data via the Xena
5 platform. *Nature Biotechnology* 38: 675-678

6 Guertin DA, Sabatini DM (2007) Defining the Role of mTOR in Cancer. *Cancer Cell* 12: 9-22

7 Guillamet E, Creus A, Ponti J, Sabbioni E, Fortaner S, Marcos R (2004) In vitro DNA damage by
8 arsenic compounds in a human lymphoblastoid cell line (TK6) assessed by the alkaline Comet
9 assay. *Mutagenesis* 19: 129-135

10 Hapach LA, Mosier JA, Wang W, Reinhart-King CA (2019) Engineered models to parse apart
11 the metastatic cascade. *npj Precision Oncology* 3: 20

12 Harvey RF, Pöyry TAA, Stoneley M, Willis AE (2019) Signaling from mTOR to eIF2α mediates
13 cell migration in response to the chemotherapeutic doxorubicin. *Science Signaling* 12:
14 eaaw6763

15 Hino N, Rossetti L, Marín-Llauradó A, Aoki K, Trepat X, Matsuda M, Hirashima T (2020) ERK-
16 Mediated Mechanochemical Waves Direct Collective Cell Polarization. *Developmental Cell* 53:
17 646-660.e648

18 Hong J, Zhou J, Fu J, He T, Qin J, Wang L, Liao L, Xu J (2011) Phosphorylation of Serine 68 of
19 Twist1 by MAPKs Stabilizes Twist1 Protein and Promotes Breast Cancer Cell Invasiveness.
20 *Cancer Research* 71: 3980-3990

Huang L, Luan T, Chen Y, Bao X, Huang Y, Fu S, Wang H, Wang J (2018) LASS2 regulates invasion and chemoresistance via ERK/Drp1 modulated mitochondrial dynamics in bladder cancer cells. *Journal of Cancer* 9: 1017-1024

Huang Q, Cao H, Zhan L, Sun X, Wang G, Li J, Guo X, Ren T, Wang Z, Lyu Y *et al* (2017) Mitochondrial fission forms a positive feedback loop with cytosolic calcium signaling pathway to promote autophagy in hepatocellular carcinoma cells. *Cancer Letters* 403: 108-118

Humphries BA, Cutter AC, Buschhaus JM, Chen Y-C, Qyli T, Palagama DSW, Eckley S, Robison TH, Bevoor A, Chiang B *et al* (2020) Enhanced mitochondrial fission suppresses signaling and metastasis in triple-negative breast cancer. *Breast Cancer Research* 22: 60

Illario M, Cavallo AL, Bayer KU, Di Matola T, Fenzi G, Rossi G, Vitale M (2003) Calcium/Calmodulin-dependent Protein Kinase II Binds to Raf-1 and Modulates Integrin-stimulated ERK Activation *. *Journal of Biological Chemistry* 278: 45101-45108

Joerger AC, Fersht AR (2007) Structure-function-rescue: the diverse nature of common p53 cancer mutants. *Oncogene* 26: 2226-2242

Kastenhuber ER, Lowe SW (2017) Putting p53 in Context. *Cell* 170: 1062-1078

Kleele T, Rey T, Winter J, Zaganelli S, Mahecic D, Perreten Lambert H, Ruberto FP, Nemir M, Wai T, Pedrazzini T *et al* (2021) Distinct fission signatures predict mitochondrial degradation or biogenesis. *Nature* 593: 435-439

Kong B, Cheng T, Qian C, Wu W, Steiger K, Cao J, Schlitter AM, Regel I, Raulefs S, Friess H *et al* (2015) Pancreas-specific activation of mTOR and loss of p53 induce tumors reminiscent of acinar cell carcinoma. *Molecular Cancer* 14: 212

Kraus F, Roy K, Pucadyil TJ, Ryan MT (2021) Function and regulation of the divisome for mitochondrial fission. *Nature* 590: 57-66

Kraus F, Ryan MT (2017) The constriction and scission machineries involved in mitochondrial fission. *Journal of Cell Science* 130: 2953-2960

Kuo M-H, Lee A-C, Hsiao S-H, Lin S-E, Chiu Y-F, Yang L-H, Yu C-C, Chiou S-H, Huang H-N, Ko J-C *et al* (2020) Cross-talk between SOX2 and TGFβ Signaling Regulates EGFR–TKI Tolerance and Lung Cancer Dissemination. *Cancer Research* 80: 4426-4438

Lakka SS, Jasti SL, Gondi C, Boyd D, Chandrasekar N, Dinh DH, Olivero WC, Gujrati M, Rao JS (2002) Downregulation of MMP-9 in ERK-mutated stable transfectants inhibits glioma invasion in vitro. *Oncogene* 21: 5601-5608

Li S, Lu J, Chen Y, Xiong N, Li L, Zhang J, Yang H, Wu C, Zeng H, Liu Y (2017) MCP-1-induced ERK/GSK-3β/Snail signaling facilitates the epithelial–mesenchymal transition and promotes the migration of MCF-7 human breast carcinoma cells. *Cellular & Molecular Immunology* 14: 621-630

Li Y, Zhang M, Dorfman RG, Pan Y, Tang D, Xu L, Zhao Z, Zhou Q, Zhou L, Wang Y *et al* (2018) SIRT2 Promotes the Migration and Invasion of Gastric Cancer through RAS/ERK/JNK/MMP-9 Pathway by Increasing PEPCK1-Related Metabolism. *Neoplasia* 20: 745-756

Liang C-C, Park AY, Guan J-L (2007) In vitro scratch assay: a convenient and inexpensive method for analysis of cell migration in vitro. *Nature Protocols* 2: 329-333

Liang J, Yang Y, Bai L, Li F, Li E (2020) DRP1 upregulation promotes pancreatic cancer growth and metastasis through increased aerobic glycolysis. *J Gastroenterol Hepatol* 35: 885-895

Lin F, Chengyao X, Qingchang L, Qianze D, Enhua W, Yan W (2015) CRKL promotes lung cancer cell invasion through ERK-MMP9 pathway. *Molecular Carcinogenesis* 54: E35-E44

Liu L, Li F, Cardelli JA, Martin KA, Blenis J, Huang S (2006) Rapamycin inhibits cell motility by suppression of mTOR-mediated S6K1 and 4E-BP1 pathways. *Oncogene* 25: 7029-7040

Maltecca F, De Stefani D, Cassina L, Consolato F, Wasilewski M, Scorrano L, Rizzuto R, Casari G (2012) Respiratory dysfunction by AFG3L2 deficiency causes decreased mitochondrial calcium uptake via organellar network fragmentation. *Human Molecular Genetics* 21: 3858-3870

Moon S-K, Cha B-Y, Kim C-H (2004) ERK1/2 mediates TNF-α-induced matrix metalloproteinase-9 expression in human vascular smooth muscle cells via the regulation of NF-κB and AP-1: Involvement of the ras dependent pathway. *Journal of Cellular Physiology* 198: 417-427

Morita M, Gravel SP, Chenard V, Sikstrom K, Zheng L, Alain T, Gandin V, Avizonis D, Arguello M, Zakaria C *et al* (2013) mTORC1 controls mitochondrial activity and biogenesis through 4E-BP-dependent translational regulation. *Cell Metab* 18: 698-711

Morita M, Prudent J, Basu K, Goyon V, Katsumura S, Hulea L, Pearl D, Siddiqui N, Strack S, McGuirk S *et al* (2017) mTOR Controls Mitochondrial Dynamics and Cell Survival via MTFP1. *Mol Cell* 67: 922-935 e925

Nagarajan D, Melo T, Deng Z, Almeida C, Zhao W (2012) ERK/GSK3β/Snail signaling mediates radiation-induced alveolar epithelial-to-mesenchymal transition. *Free Radical Biology and Medicine* 52: 983-992

Nakamura Y, Arakawa H (2017) Discovery of Mieap-regulated mitochondrial quality control as a new function of tumor suppressor p53. *Cancer Science* 108: 809-817

1 Nunnari J, Suomalainen A (2012) Mitochondria: in sickness and in health. *Cell* 148: 1145-1159

2 Park J-H, Zhuang J, Li J, Hwang PM (2016) p53 as guardian of the mitochondrial genome.
3 *FEBS Letters* 590: 924-934

4 Pernas L, Scorrano L (2016) Mito-Morphosis: Mitochondrial Fusion, Fission, and Cristae
5 Remodeling as Key Mediators of Cellular Function. *Annual Review of Physiology* 78: 505-531

6 Ponte S, Carvalho L, Gagliardi M, Campos I, Oliveira PJ, Jacinto A (2020) Drp1-mediated
7 mitochondrial fission regulates calcium and F-actin dynamics during wound healing. *Biology*
8 *Open* 9

9 Popov L-D (2020) Mitochondrial biogenesis: An update. *Journal of Cellular and Molecular*
10 *Medicine* 24: 4892-4899

11 Powell E, Piwnica-Worms D, Piwnica-Worms H (2014) Contribution of p53 to Metastasis.
12 *Cancer Discovery* 4: 405-414

13 Prevarskaya N, Skryma R, Shuba Y (2011) Calcium in tumour metastasis: new roles for known
14 actors. *Nature Reviews Cancer* 11: 609-618

15 Quintero-Fabián S, Arreola R, Becerril-Villanueva E, Torres-Romero JC, Arana-Argáez V, Lara-
16 Riegos J, Ramírez-Camacho MA, Alvarez-Sánchez ME (2019) Role of Matrix
17 Metalloproteinases in Angiogenesis and Cancer. *Frontiers in Oncology* 9

18 Robinson DR, Wu Y-M, Lonigro RJ, Vats P, Cobain E, Everett J, Cao X, Rabban E, Kumar-
19 Sinha C, Raymond V *et al* (2017) Integrative clinical genomics of metastatic cancer. *Nature* 548:
20 297-303

Schwerdtle T, Walter I, Mackiw I, Hartwig A (2003) Induction of oxidative DNA damage by arsenite and its trivalent and pentavalent methylated metabolites in cultured human cells and isolated DNA. *Carcinogenesis* 24: 967-974

Stambolic V, MacPherson D, Sas D, Lin Y, Snow B, Jang Y, Benchimol S, Mak TW (2001) Regulation of PTEN Transcription by p53. *Molecular Cell* 8: 317-325

Sun X, Cao H, Zhan L, Yin C, Wang G, Liang P, Li J, Wang Z, Liu B, Huang Q *et al* (2018) Mitochondrial fission promotes cell migration by Ca(2+) /CaMKII/ERK/FAK pathway in hepatocellular carcinoma. *Liver Int* 38: 1263-1272

Tanimura S, Takeda K (2017) ERK signalling as a regulator of cell motility. *The Journal of Biochemistry* 162: 145-154

Tondera D, Czauderna F, Paulick K, Schwarzer R, Kaufmann J, Santel A (2005) The mitochondrial protein MTP18 contributes to mitochondrial fission in mammalian cells. *Journal of Cell Science* 118: 3049-3059

Tsai F-C, Seki A, Yang HW, Hayer A, Carrasco S, Malmersjö S, Meyer T (2014) A polarized Ca2+, diacylglycerol and STIM1 signalling system regulates directed cell migration. *Nature Cell Biology* 16: 133-144

Twig G, Elorza A, Molina AJA, Mohamed H, Wikstrom JD, Walzer G, Stiles L, Haigh SE, Katz S, Las G *et al* (2008) Fission and selective fusion govern mitochondrial segregation and elimination by autophagy. *The EMBO Journal* 27: 433-446

Virtakoivu R, Mai A, Mattila E, De Franceschi N, Imanishi SY, Corthals G, Kaukonen R, Saari M, Cheng F, Torvaldson E *et al* (2015) Vimentin–ERK Signaling Uncouples Slug Gene Regulatory Function. *Cancer Research* 75: 2349-2362

1 Vousden KH, Ryan KM (2009) p53 and metabolism. *Nature Reviews Cancer* 9: 691-700

2 Wang T, Liao Y, Sun Q, Tang H, Wang G, Zhao F, Jin Y (2017a) Upregulation of Matrix
3 Metalloproteinase-9 in Primary Cultured Rat Astrocytes Induced by 2-Chloroethanol Via MAPK
4 Signal Pathways. *Frontiers in Cellular Neuroscience* 11

5 Wang Y, Subramanian M, Yurdagul A, Jr., Barbosa-Lorenzi VC, Cai B, de Juan-Sanz J, Ryan
6 TA, Nomura M, Maxfield FR, Tabas I (2017b) Mitochondrial Fission Promotes the Continued
7 Clearance of Apoptotic Cells by Macrophages. *Cell* 171: 331-345.e322

8 Weiss MB, Abel EV, Mayberry MM, Basile KJ, Berger AC, Aplin AE (2012) TWIST1 Is an
9 ERK1/2 Effector That Promotes Invasion and Regulates MMP-1 Expression in Human
10 Melanoma Cells. *Cancer Research* 72: 6382-6392

11 Westermann B (2010) Mitochondrial fusion and fission in cell life and death. *Nature Reviews*
12 *Molecular Cell Biology* 11: 872

13 White C (2017) The Regulation of Tumor Cell Invasion and Metastasis by Endoplasmic
14 Reticulum-to-Mitochondrial Ca2+ Transfer. *Frontiers in Oncology* 7

15 Yao J, Xiong S, Klos K, Nguyen N, Grijalva R, Li P, Yu D (2001) Multiple signaling pathways
16 involved in activation of matrix metalloproteinase-9 (MMP-9) by heregulin-β1 in human breast
17 cancer cells. *Oncogene* 20: 8066-8074

18 Yilmaz M, Christofori G (2010) Mechanisms of motility in metastasizing cells. *Mol Cancer Res* 8:
19 629-642

20 Yin M, Lu Q, Liu X, Wang T, Liu Y, Chen L (2016) Silencing Drp1 inhibits glioma cells
21 proliferation and invasion by RHOA/ ROCK1 pathway. *Biochem Biophys Res Commun* 478:
22 663-668

Zehir A, Benayed R, Shah RH, Syed A, Middha S, Kim HR, Srinivasan P, Gao J, Chakravarty D, Devlin SM *et al* (2017) Mutational landscape of metastatic cancer revealed from prospective clinical sequencing of 10,000 patients. *Nat Med* 23: 703-713

Zhang Q, Zhang Y, Chen Y, Qian J, Zhang X, Yu K (2019) A Novel mTORC1/2 Inhibitor (MTI-31) Inhibits Tumor Growth, Epithelial–Mesenchymal Transition, Metastases, and Improves Antitumor Immunity in Preclinical Models of Lung Cancer. *Clinical Cancer Research* 25: 3630-3642

Zhang Y, Li H, Chang H, Du L, Hai J, Geng X, Yan X (2018) MTP18 overexpression contributes to tumor growth and metastasis and associates with poor survival in hepatocellular carcinoma. *Cell Death & Disease* 9: 956

Zhang Z, Li T-E, Chen M, Xu D, Zhu Y, Hu B-Y, Lin Z-F, Pan J-J, Wang X, Wu C *et al* (2020) MFN1-dependent alteration of mitochondrial dynamics drives hepatocellular carcinoma metastasis by glucose metabolic reprogramming. *British Journal of Cancer* 122: 209-220

Zhao J, Zhang J, Yu M, Xie Y, Huang Y, Wolff DW, Abel PW, Tu Y (2013) Mitochondrial dynamics regulates migration and invasion of breast cancer cells. *Oncogene* 32: 4814-4824

Zhou S, Kachhap S, Singh KK (2003) Mitochondrial impairment in p53-deficient human cancer cells. *Mutagenesis* 18: 287-292

Figure legends

Figure 1. Downregulation of WT p53 expression is associated with aggressive tumor phenotypes and poor prognosis

A, B. Contingency analysis of the associations between the presence of *TP53* mutations and the probabilities of metastases to (A) lymph nodes and (B) distant organs. N0, lymph node-negative; N1+, lymph-node-positive.

C. Kaplan-Meier analysis of overall survival in cancer patients having WT and MUT *TP53*.

D, E. p53 protein expression of patients having WT *TP53* (D) with N0 and N1+ and (E) with stage I+II and III+IV tumors.

F. Kaplan-Meier analysis of overall survival in *TP53* WT cancer patients with low and high p53 protein levels.

G. Phase-contrast imaging of control (siCtrl) and p53-silenced (sip53-1 and sip53-2) A549 and MCF-7 cells. Scale bar: 100 μm.

H, I. Migration distance (G) and representative trajectories (H) of siCtrl (n = 28) and sip53 (n = 14) A549 cells.

K. Transwell assays for siCtrl, sip53-1, and sip53-2 A549 cells. Scale bar: 100 μm.

Error bars represent mean ± SEM (D and E) or SD (K). Data were analyzed by Fisher's exact test (A and B), log-rank test (C and F), or two-tailed unpaired Student's t test (D, E, H, and K).

Figure 2. p53 silencing amplifies mitochondrial fission has diagnostic and clinical implications

A, B. Representative images (A) and quantification (B) of mitochondrial morphology in siCtrl (n = 222) and sip53 (n = 230) A549 cells. Boxed regions in (A) are shown enlarged in the bottom panels. Scale bar: 20 μm. (B) Representative images for each mitochondrial morphology type are shown in the bottom panels.

C, D. Drp1 mRNA expression in (C) N0 and N1+ or (D) stage I+II and III+IV tumors.

E. Kaplan-Meier analysis of overall survival in cancer patients with low and high Drp1 mRNA levels.

Error bars represent mean ± SD (B) or SEM (C and D). Data were analyzed by two-tailed unpaired Student's t test (B, C, and D) or log-rank test (E). ***, $p < 0.001$; ****, $p < 0.0001$.

Figure 3. p53 elevation promotes mitochondrial elongation accompanied by attenuated invasive cell migration

A. Immunoblot of p53 in siCtrl and sip53 A549 cells with and without 20 μM SA treatment for 24 h. GAPDH was used as a loading control.

B, C. Representative images (B) and quantification (C) of mitochondrial morphology in siCtrl (n = 223), siCtrl+SA (n = 211), sip53 (n = 205), and sip53+SA (n = 218) A549 cells. Boxed regions in (B) are shown enlarged in the bottom panels. Scale bar: 20 μm.

D, E. Migration distance (D) and representative trajectories (E) of siCtrl (n= 29), siCtrl+SA (n = 17), sip53 (n = 13), and sip53+SA (n = 15) A549 cells.

F, G. Transwell assays for (F) siCtrl, siCtrl+SA, sip53, and sip53+SA A549 cells or (G) control (Ctrl) and p53-overexpressing (p53) H1299 cells. Scale bar: 100 μm.

Error bars represent mean ±SD. Data were analyzed by two-tailed unpaired Student's t test. **, $p < 0.01$; ****, $p < 0.0001$.

Figure 4. p53 alleviates Drp1-mediated mitochondrial fission and thereby restrains cell migration and invasion

A. Immunoblot of the indicated proteins in siCtrl, sip53, and p53/Drp1 double-knockdown (sip53+siDrp1) A549 cells with and without 20 μM SA treatment for 24 h. GAPDH was used as a loading control.

B. Quantification of levels of Drp1, p-Drp1 (S637), and p-Drp1 (S616) in Fig 4A.

C. Immunoblot of the indicated proteins in siCtrl and sip53 MCF-7 cells with and without 20 μM SA treatment for 24 h. GAPDH was used as a loading control.

D, E. Representative images (D) and quantification (E) of mitochondrial morphology in siCtrl (n = 226), siCtrl+SA (n = 232), sip53 (n = 205), sip53+SA (n = 214), sip53+siDrp1 (n = 230), and sip53+siDrp1+SA (n = 214) A549 cells. Boxed regions in (D) are shown enlarged in the bottom panels. Scale bar: 20 μm.

F. Transwell assays for siCtrl, sip53, and sip53+siDrp1 A549 cells.

Error bars represent mean ± SD. Data were analyzed by two-tailed unpaired Student's t test. ****, $p < 0.0001$.

Figure 5. p53 diminishes mTORC1-controlled MTFP1 protein levels to attenuate Drp1-driven mitochondrial fission and invasive cell migration

A. Correlations between the RPPA levels of p53 and the indicated proteins (n = 7694 samples).

B. Immunoblot of the indicated proteins in siCtrl, sip53, p53/mTOR double-knockdown (sip53+simTOR), and p53/MTFP1 double-knockdown (sip53+siMTFP1) A549 cells with and without 20 μM SA treatment for 24 h. GAPDH was used as a loading control.

C, D. Representative images (C) and quantification (D) of mitochondrial morphology in siCtrl (n = 203), siCtrl+SA (n = 207), sip53 (n = 200), sip53+SA (n = 213), sip53+simTOR (n = 234), sip53+simTOR+SA (n = 209), sip53+siMTFP1 (n = 214), and sip53+siMTFP1+SA (n = 213) A549 cells. Boxed regions in (C) are shown enlarged in the bottom panels of each group. Scale bar: 20 μm.

E. Transwell assays for siCtrl, sip53, sip53+simTOR, and sip53+siMTFP1 A549 cells.

Error bars represent mean ± SD. Data were analyzed by two-tailed unpaired Student's t test. ****, $p < 0.0001$.

Figure 6. Activation of mTORC1/MTFP1/Drp1/ERK signaling axis is required for increased MMP9 expression and cancer dissemination upon WT p53 loss

A. Correlations between the RPPA levels of p-ERK1/2 (T202/Y204) and the indicated proteins (n = 7694 samples).

B. Immunoblot of the indicated proteins in siCtrl, sip53, and PD98059-treated sip53 (sip53+PD98059) A549 cells with and without 20 μM SA treatment for 24 h. GAPDH was used as a loading control.

C. Transwell assays for siCtrl, sip53, and sip53+ PD98059 A549 cells.

D. qRT-PCR analysis of MMP9 mRNA expression in siCtrl, sip53, sip53+PD98059, sip53+siDrp1, sip53+simTOR, and sip53+siMTFP1 A549 cells.

E. MMP9 mRNA expression in tumors having WT and MUT *TP53*.

F. Correlation between p53 protein levels and MMP9 mRNA levels in tumors having WT *TP53* (n = 4538 samples).

G, H. MMP9 mRNA expression in (G) N0 and N1+ or (H) stage I+II and III+IV tumors.

I. Kaplan-Meier analysis of the overall survival in cancer patients with low and high MMP9 mRNA expression levels (left). Patients were further divided into MMP9 mRNA high / WT p53 protein low and MMP9 mRNA low / WT p53 protein high groups (right).

Error bars represent mean ± SD (C and D) or SEM (E, G, and H). Data were analyzed by two-tailed unpaired Student's t test (C, D, E, G, and H) or log-rank test (I).

Figure 7. Schematic model of how p53 modulates mitochondrial dynamics to constrain the morphologic switch, MMP-9 expression, and invasive cell migration

WT p53 suppresses mTORC1-directed MTFP1 protein expression and the aberrant phosphorylation of Drp1 at the pro-fission site S616, maintaining the predominantly intermediate state of mitochondria, and thereby constraining ERK1/2-mediated cell migration and invasion. Loss of WT p53 elevates mTORC1 activity, MTFP1 protein levels, and the phosphorylation of S616 on Drp1, shifting mitochondrial dynamics toward fission to promote ERK1/2 activation and resulting in EMT-like changes in cell morphology, increased MMP9 expression, and cell dissemination.

Expanded View Figure legends

Figure EV1. Reduced WT p53 expression is associated with EMT signatures and accelerated cell migration (related to Fig 1)

A. p53 mRNA levels in primary and distant metastatic melanoma.

B-D. Correlations between p53 protein levels and (B) Twist1, (C) Slug, and (D) Snail mRNA levels in tumors having WT *TP53* (n = 4538 samples).

E. Twist1, Slug, and Snail mRNA expression in tumors having WT and MUT *TP53*.

F. Quantification (left) and representative images (right) of the area in a wound-healing assay covered by A549 cells transfected with siCtrl or sip53. Scale bar: 100 μm.

Error bars represent mean ± SEM (A and E) or SD (F). Data were analyzed by two-tailed unpaired Student's t test.

Figure EV2. Elevated Drp1 expression correlates with EMT signatures and distant metastases (related to Fig 2)

A, B. Correlations between Drp1 and (A) Twist1 and (B) Slug mRNA levels (n=10,071 samples).

C. Drp1 mRNA levels in primary and distant metastatic melanoma.

Error bars represent mean ± SEM. Data were analyzed by two-tailed unpaired Student's t test.

Figure EV3. Effects of p53 on cell viability, mitochondrial function, and cell migration (related to Fig 3)

A. Immunoblot of p53 in A549 cells treated with SA at the indicated concentrations for 24 h. GAPDH was used as a loading control.

B, C. The viability of A549 cells treated with SA at the indicated concentrations for 24 h was measured by (B) colony formation assay or (C) MTT assay.

D. Cell viability was measured by MTT assay in siCtrl- and sip53-transfected A549 cells with and without 20 μM SA treatment for 24 h.

E, F. Flow cytometry analysis of (E) MMP or (F) mitochondrial ROS levels in siCtrl, siCtrl+SA, sip53, and sip53+SA A549 cells.

G. Quantification (left) and representative images (right) of the area in a wound-healing assay covered by Ctrl and p53-expressing H1299 cells. Scale bar: 100 μm.

Error bars represent mean ± SD. Data were analyzed by two-tailed unpaired Student's t test.

Figure EV4. p53 suppresses cell motility by inhibiting the pro-fission phosphorylation of Drp1 (related to Fig 4)

A. qRT-PCR analysis of the mRNA levels of p53 and genes involved in mitochondrial fusion and fission in sip53 A549 cells. Results are expressed relative to those in siCtrl A549 cells (dashed line).

B. Immunoblot of the indicated proteins in Ctrl and p53 H1299 cells with and without 20 μM SA treatment for 24 h. GAPDH was used as a loading control.

C. Quantification of the levels of Drp1, p-Drp1 (S637), and p-Drp1 (S616) in Figure S4B.

D, E. Migration distance (D) and representative trajectories (E) of siCtrl (n = 29), siCtrl+SA (n = 17), sip53 (n = 13), sip53+SA (n = 15), sip53+siDrp1 (n = 24), and sip53+siDrp1+SA (n = 24) A549 cells.

F. Quantification (left) and representative images (right) of the area in a wound-healing assay covered by siCtrl, siCtrl+SA, sip53, sip53+SA, sip53+siDrp1, and sip53+siDrp1+SA A549 cells. Scale bar: 100 μm.

Error bars represent mean ± SD. Data were analyzed by two-tailed unpaired Student's t test. ****, $p < 0.0001$; ns, not significant.

Figure EV5. p53 transcriptional activity participates in regulating mTORC1-controlled MTFP1 protein levels affecting cell motility (related to Fig 5)

A. Immunoblot of the indicated proteins in control (Ctrl) and PFT-α-treated (PFT-α) A549 cells with and without 20 μM SA treatment for 24 h. GAPDH was used as a loading control.

B. qRT-PCR analysis of the mRNA levels of p53 and p53 downstream target genes in sip53 A549 cells. Results were expressed relative to those in siCtrl A549 cells (dashed line).

C. qRT-PCR analysis of mRNA expression of MTFP1 in siCtrl and sip53 A549 cells with and without 20 μM SA treatment for 24 h.

D, E. Migration distance (D) and representative trajectories (E) of siCtrl (n = 28), siCtrl+SA (n = 17), sip53 (n = 13), sip53+SA (n = 14), sip53+simTOR (n = 33), sip53+simTOR+SA (n = 28), sip53+siMTFP1 (n = 32), and sip53+siMTFP1+SA (n = 20) A549 cells.

Error bars represent mean ± SD. Data were analyzed by two-tailed unpaired Student's t test. ***, $p < 0.001$; ****, $p < 0.0001$.

Figure EV6. p53 controls cell motility and MMP9 expression through mTOR/MTFP1/Drp1/ERK signaling axis (related to Fig 6)

A. Phase-contrast imaging of siCtrl, sip53, sip53+siDrp1, sip53+simTOR, sip53+siMTFP1, and sip53+PD98059 A549 and MCF-7 cells. Scale bar: 100 μm.

B, C. Migration distance (B) and representative trajectories (C) of siCtrl (n = 31), siCtrl+SA (n = 19), sip53 (n = 13), sip53+SA (n = 14), sip53+ PD98059 (n = 20), and sip53+PD98059+SA (n = 35) A549 cells.

D. qRT-PCR analysis of MMP9 mRNA expression in siCtrl, sip53, sip53+PD98059, sip53+siDrp1, sip53+simTOR, and sip53+siMTFP1 MCF-7 cells.

E. MMP9 mRNA levels in primary and distant metastatic melanoma.

Error bars represent mean ± SD (D) or SEM (E). Data were analyzed by two-tailed unpaired Student's t test.

Expanded View tables

Table EV1. siRNA sequences (related to Materials and Methods)

Target protein	Oligo ID	Sequence (5'-3')
p53	VHS40367	Sense: CCAGUGGUAAUCUACUGGGACGGAA
		Antisense: UUCCGUCCCAGUAGAUUACCACUGG
p53	VHS40366	Sense: CCAUCCACUACAACUACAUGUGUAA
		Antisense: UUACACAUGUAGUUGUAGUGGAUGG
Drp1	HSS115288	Sense: CCUGCUUUAUUUGUGCCUGAGGUUU
		Antisense: AAACCUCAGGCACAAAUAAAGCAGG
mTOR	HSS103825	Sense: AGGACGCUCACAUUGCUAGAUGUGG
		Antisense: CCACAUCUAGCAAUGUGAGCGUCCU
MTFP1	HSS182106	Sense: GGGAUACCUGGGCUAUGCCAAUGAG
		Antisense: CUCAUUGGCAUAGCCCAGGUAUCGC

Table EV2. List of primers used for qRT-PCR (related to Materials and Methods)

Target protein	Sequence (5'-3')
p53	Forward: AAGGAAATTTGCGTGTGGAGT
	Reverse: AAAGCTGTTCCGTCCCAGTA
Mfn1	Forward: GAGGTGCTATCTCGGAGACAC
	Reverse: GCCAATCCCACTAGGGAGAAC
Mfn2	Forward: CACATGGAGCGTTGTACCAG
	Reverse: TTGAGCACCTCCTTAGCAGAC
Opa1	Forward: TGTGAGGTCTGCCAGTCTTTA
	Reverse: TGTCCTTAATTGGGGTCGTTG
Drp1	Forward: ACCCGGAGACCTCTCATTCT
	Reverse: TGACAACGTTGGGTGAAAAA
Fis1	Forward: GATGACATCCGTAAAGGCATCG
	Reverse: AGAAGACGTAATCCCGCTGTT
Mff	Forward: CACCACCTCGTGTACTTACGC
	Reverse: GTCTGCCAACTGCTCGGATTT
MIEF1	Forward: CACGGCCATTGACTTTGTGC
	Reverse: TCGTACATCCGCTTAACTGCC
PTEN	Forward: AGTTCCCTCAGCCGTTACCT
	Reverse: AGGTTTCCTCTGGTCCTGGT
AMPKβ1	Forward: TCCGATGTGTCTGAGCTGTC
	Reverse: GTTCAGCATGACGTGATTGG
Sestrin1	Forward: AGCCCATAGACCTTGGCTTA
	Reverse: TCCACACTGTGATTGCCATT
Sestrin2	Forward: TGCTGTGCTTTGTGGAAGAC
	Reverse: GCTGCCTGGAACTTCTCATC
TSC2	Forward: TGCAAGCCGTCTTCCACAT
	Reverse: ATGGACACAAAGTCGTTGC
MTFP1	Forward: CCATCCCCATCATTATCCAC
	Reverse: TTCCCCACTGTTGGGTAGAG
GAPDH	Forward: TGCACCACCAACTGCTTAGC
	Reverse: GGCATGGACTGTGGTCATGAG

Main Figures

Figure 1

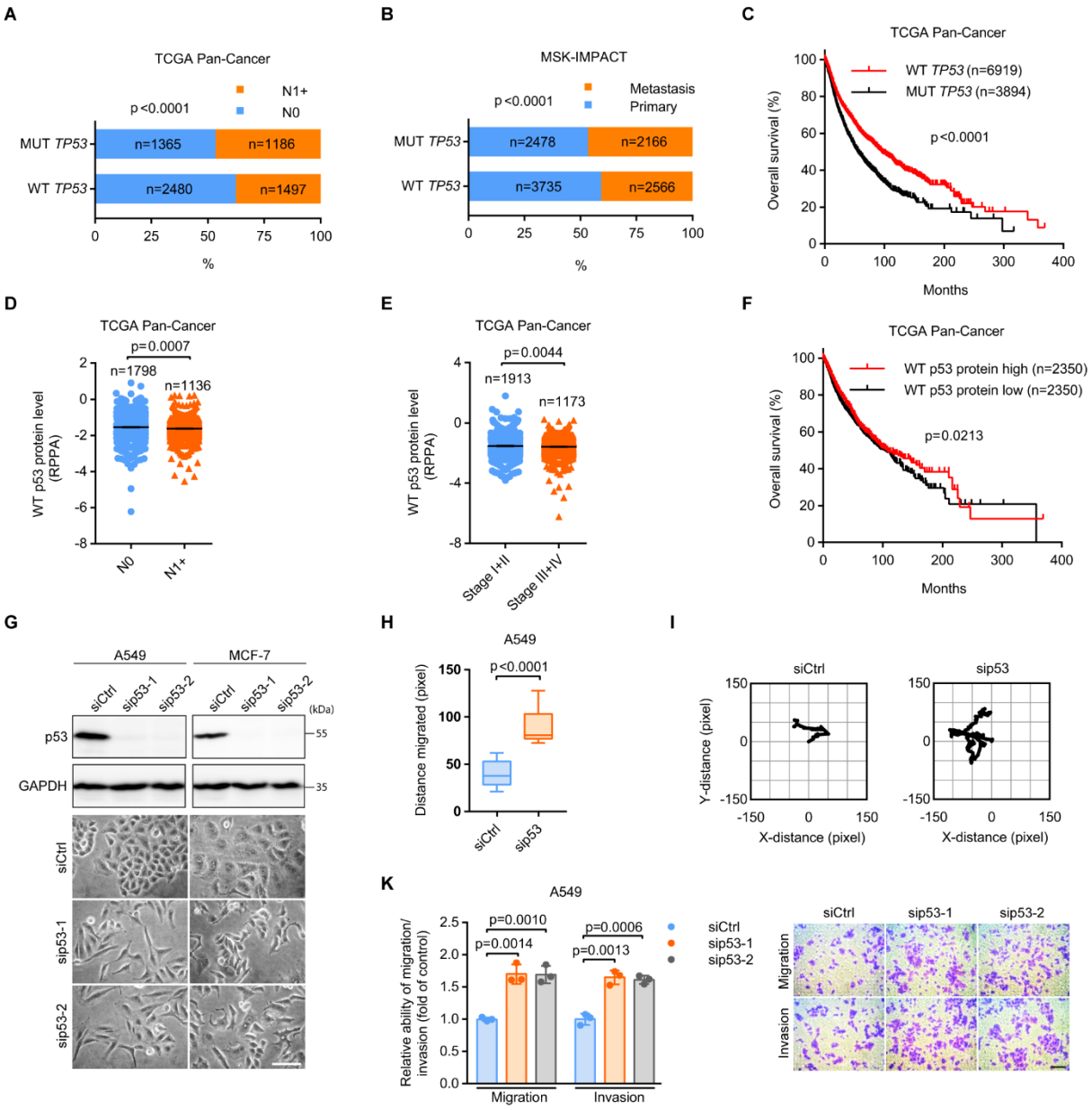

Figure 2

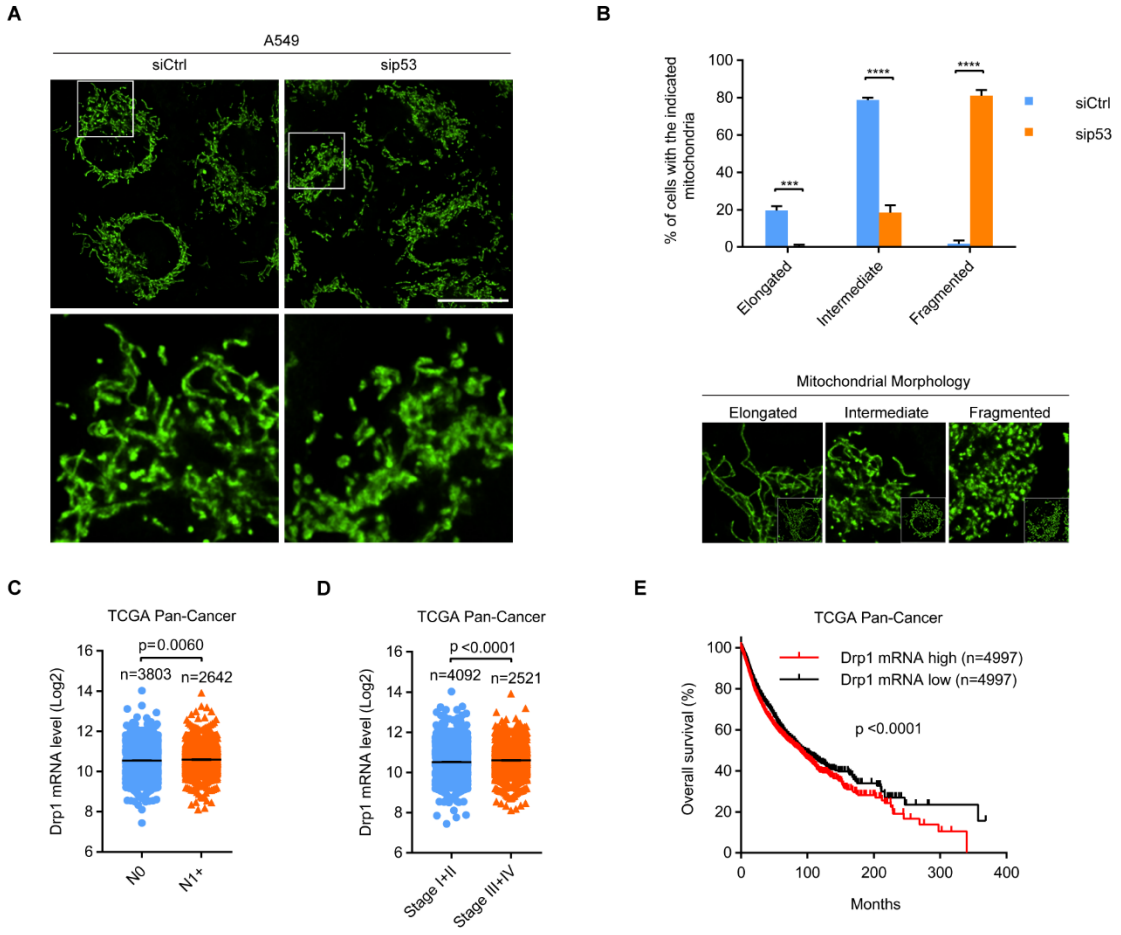

Figure 3

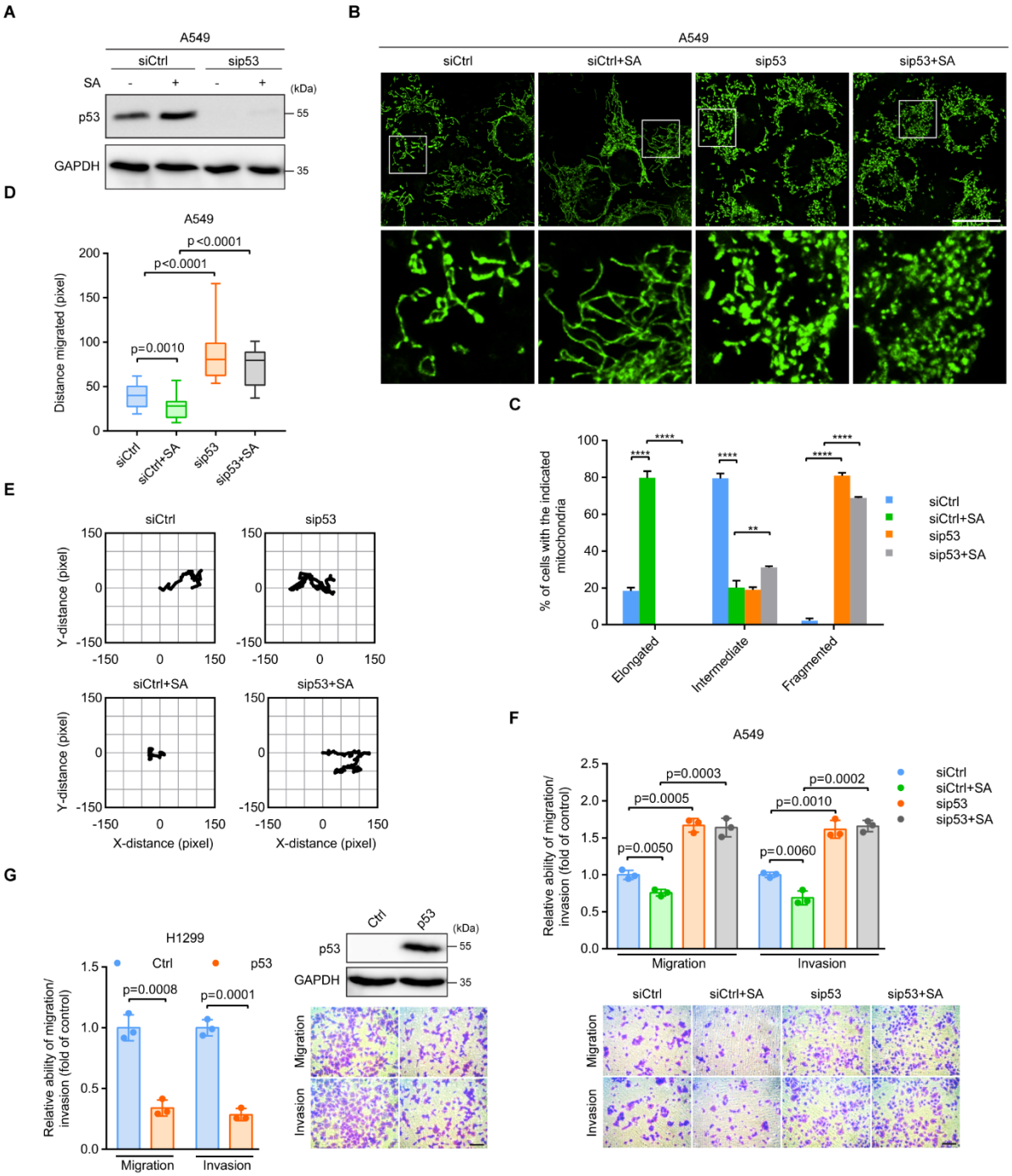

Figure 4

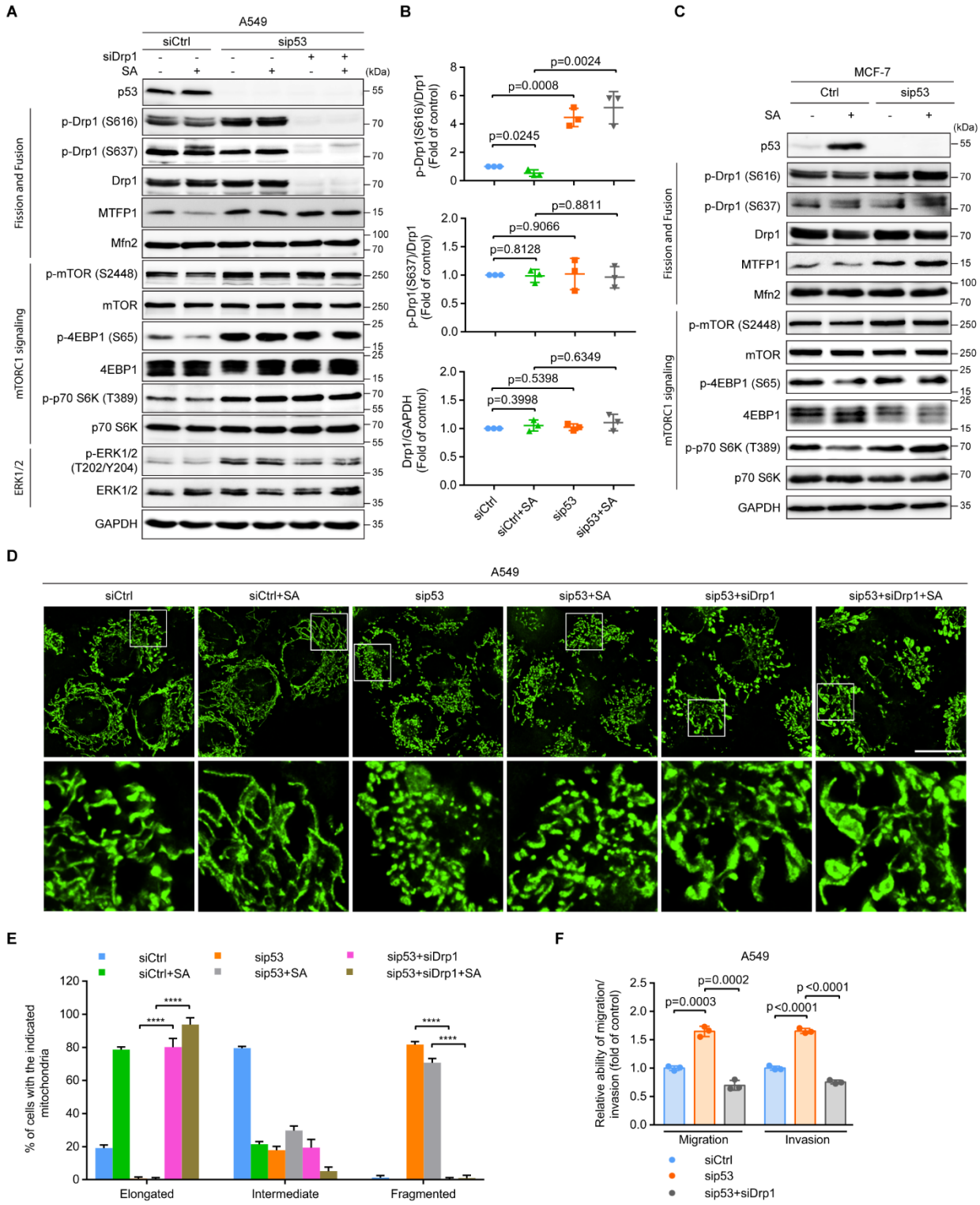

Figure 5

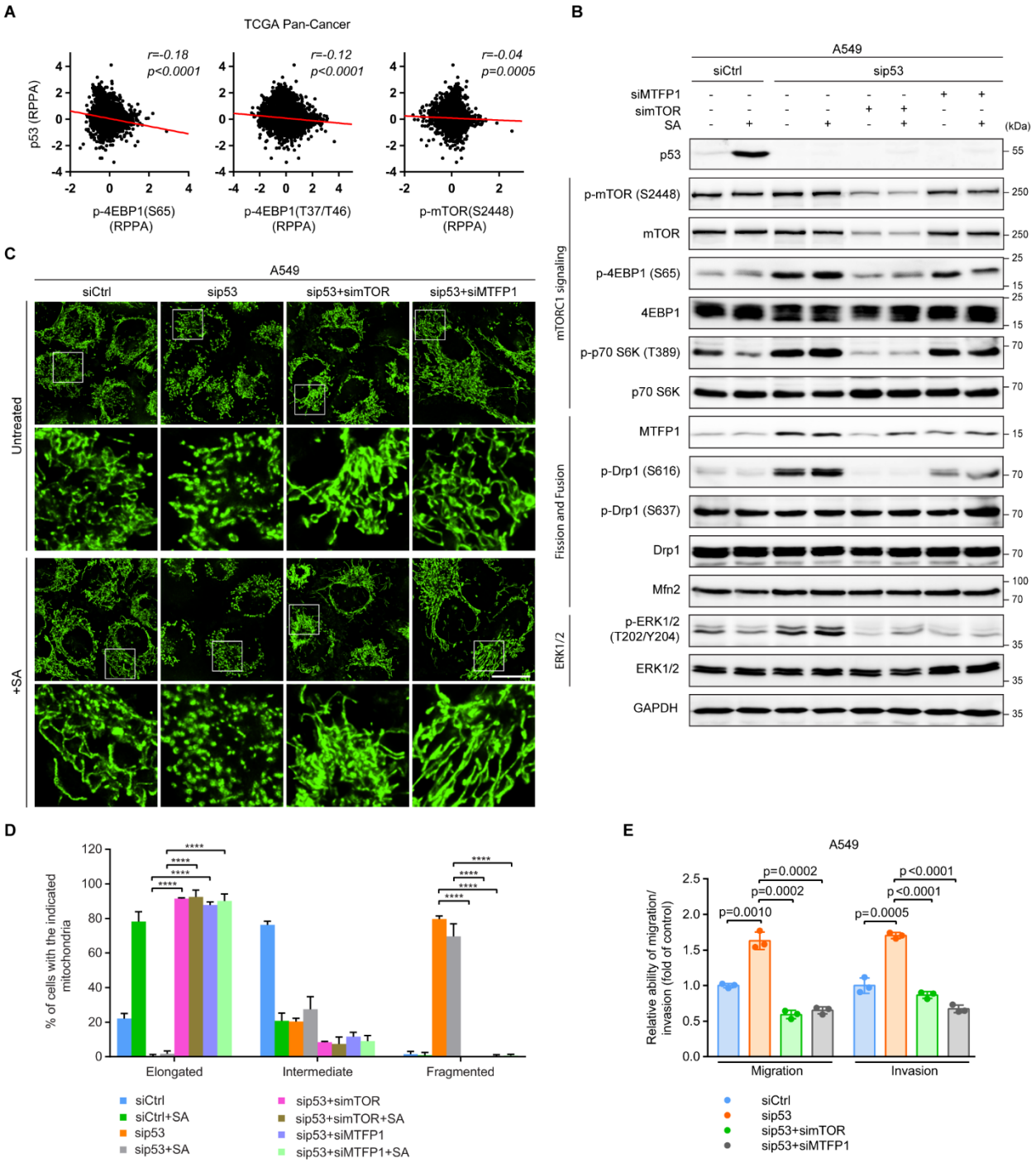

Figure 6

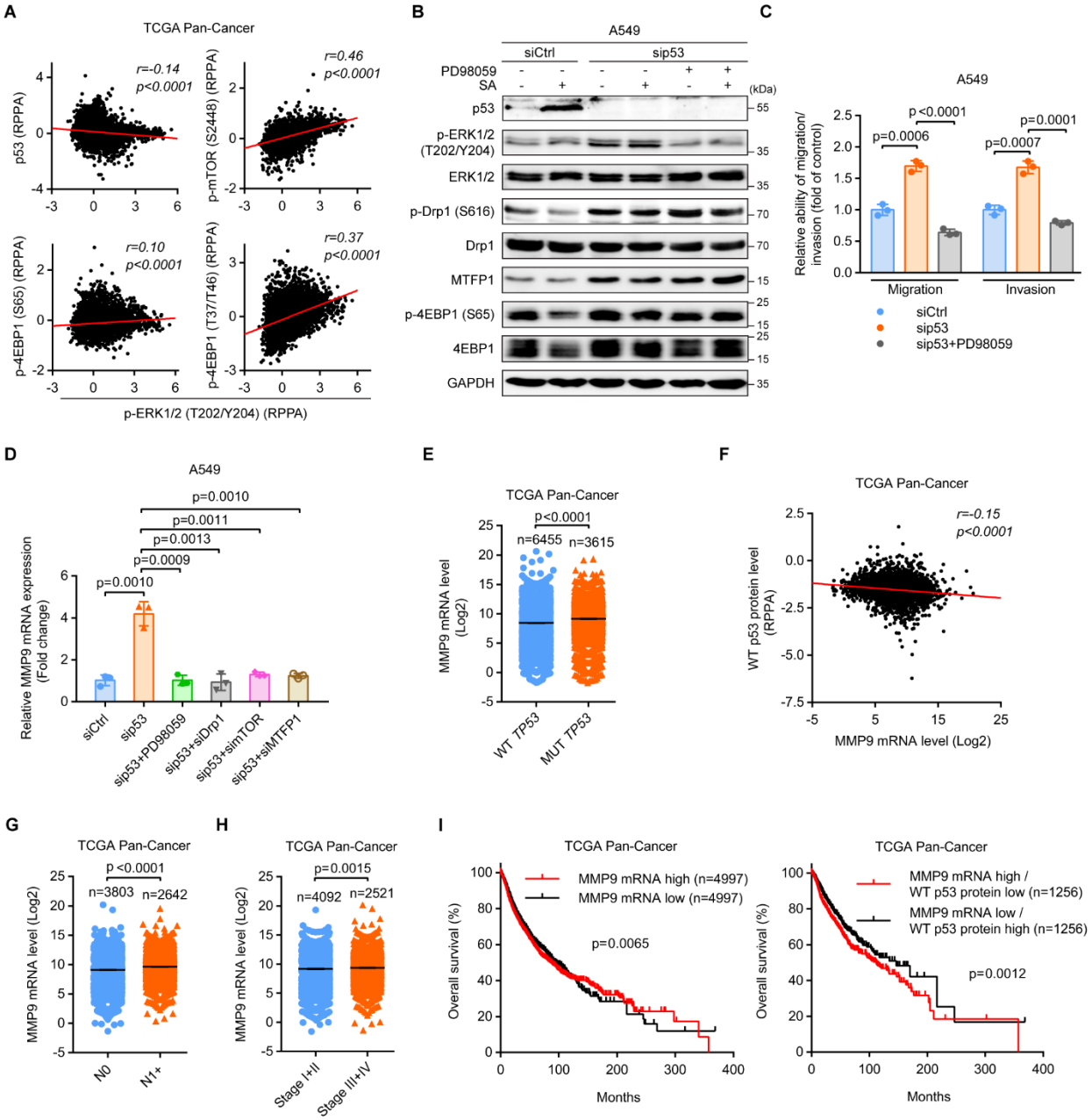

Figure 7

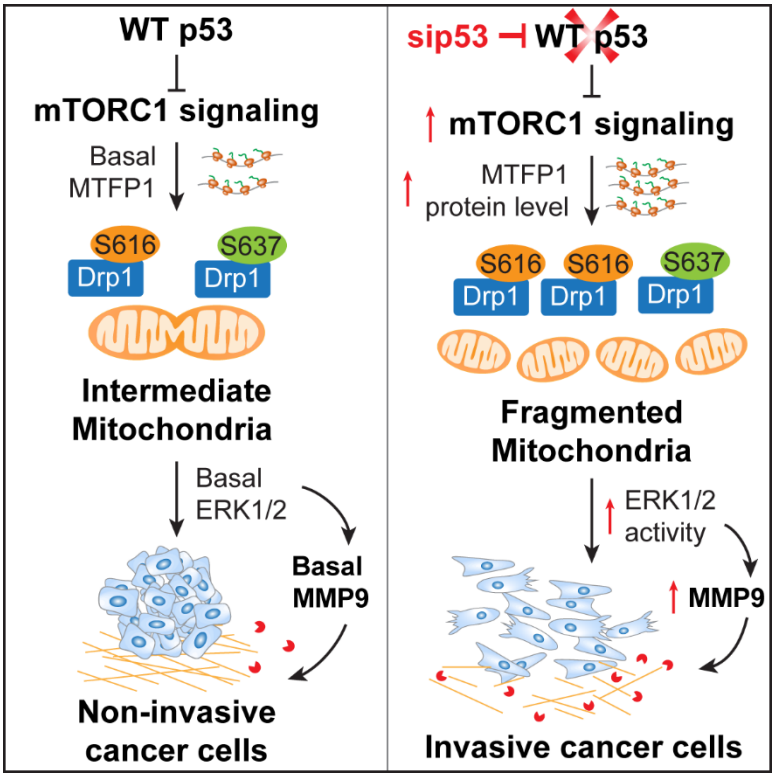

Expanded View Figures

Figure EV1

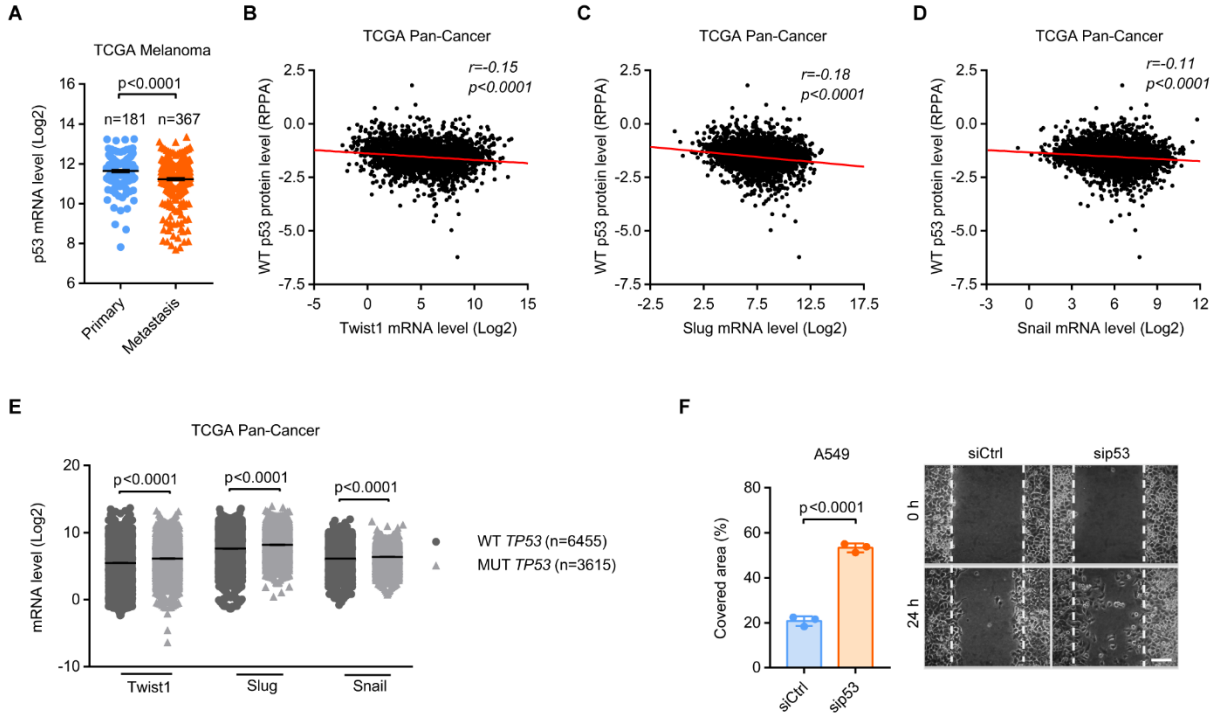

Figure EV2

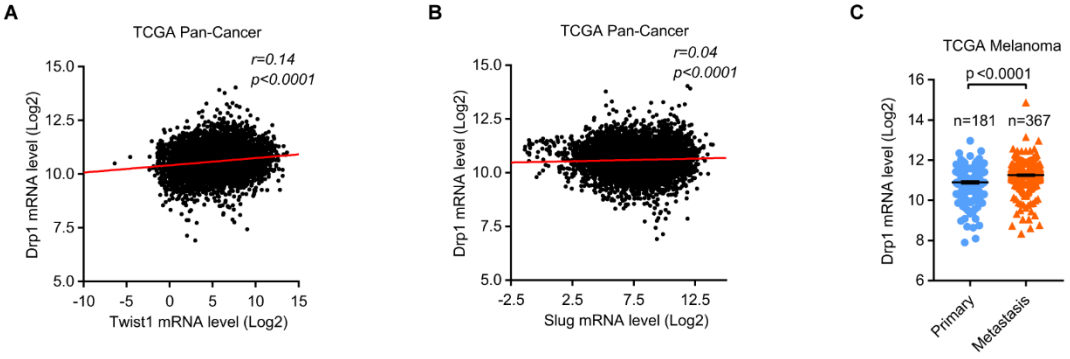

Figure EV3

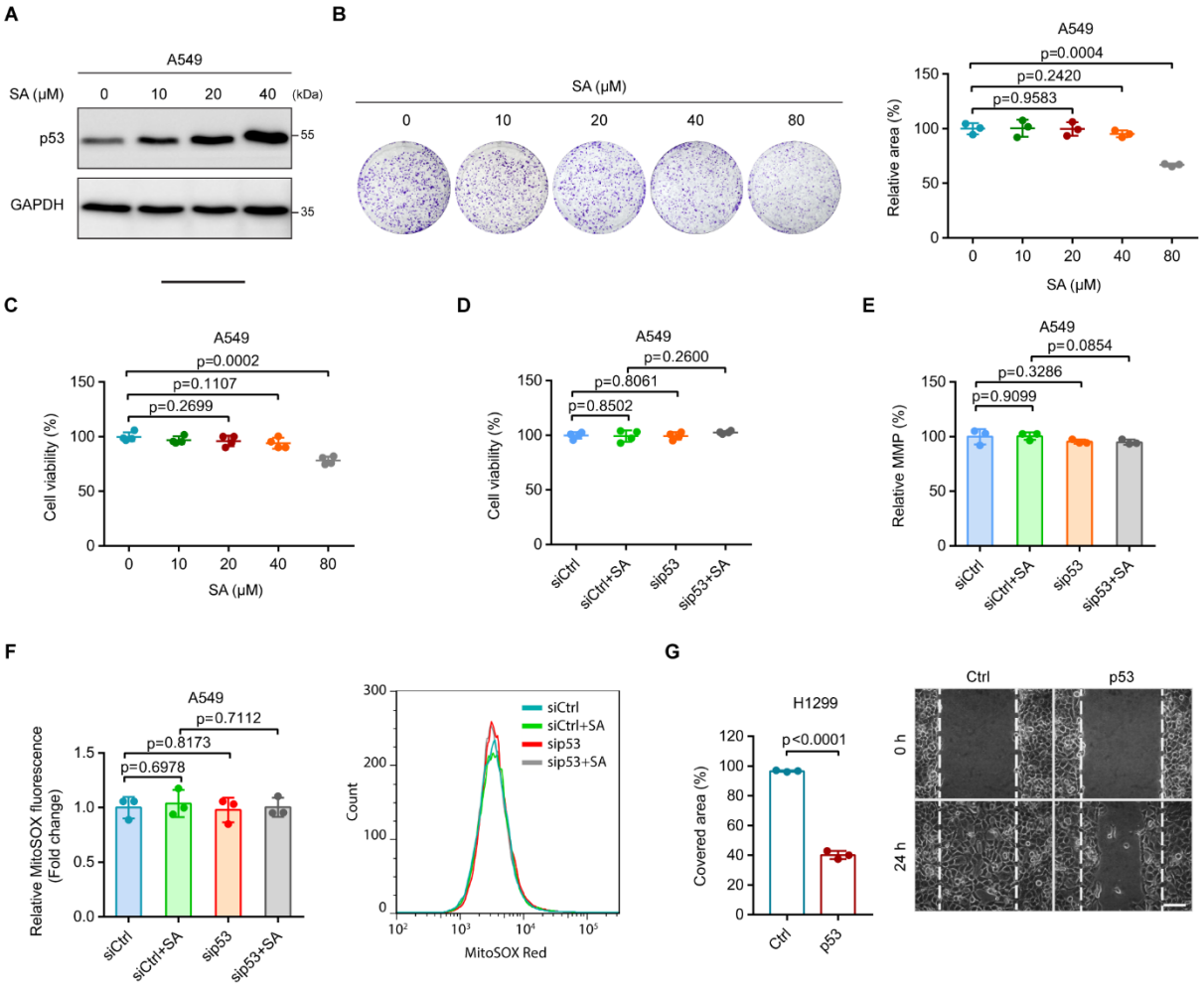

Figure EV4

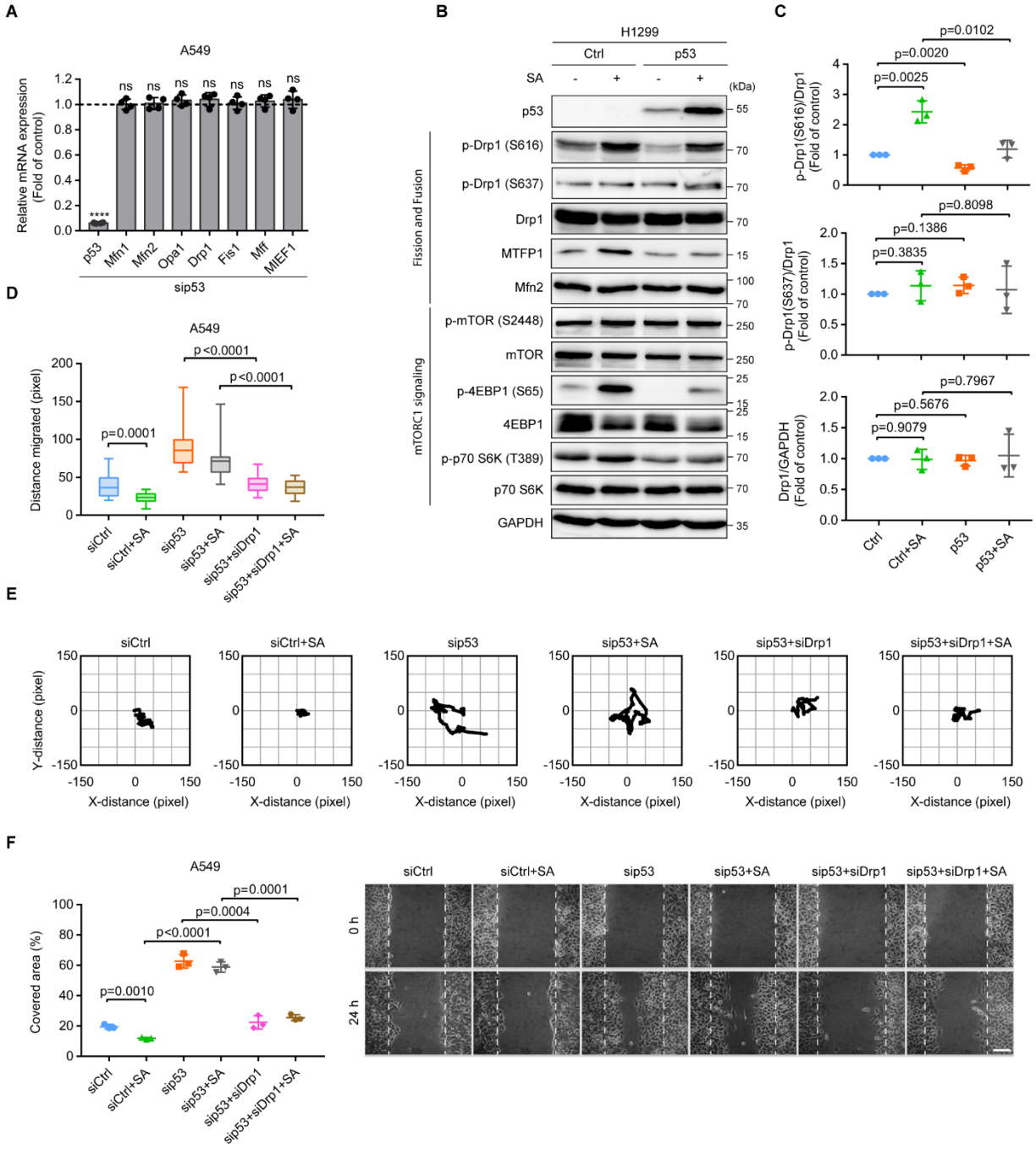

Figure EV5

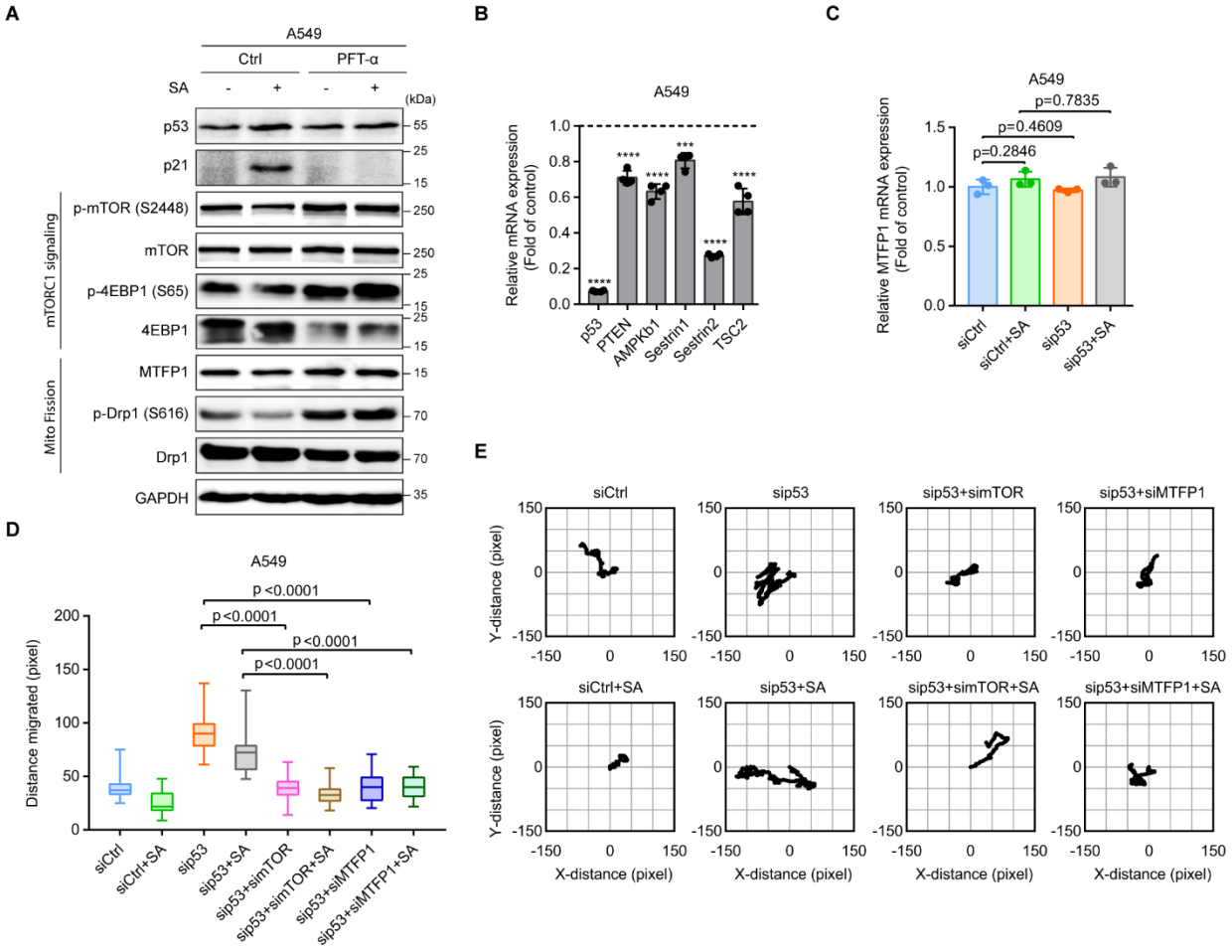

Figure EV6